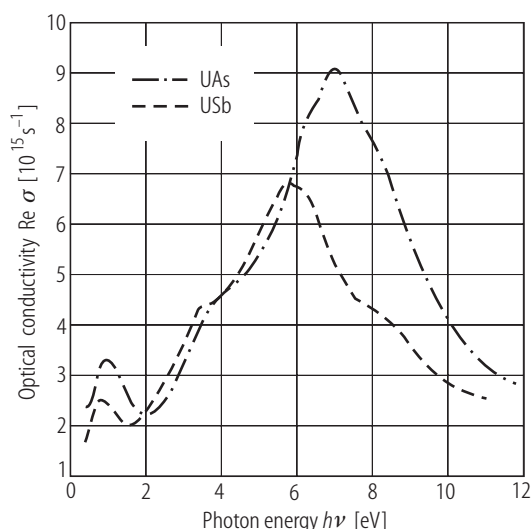
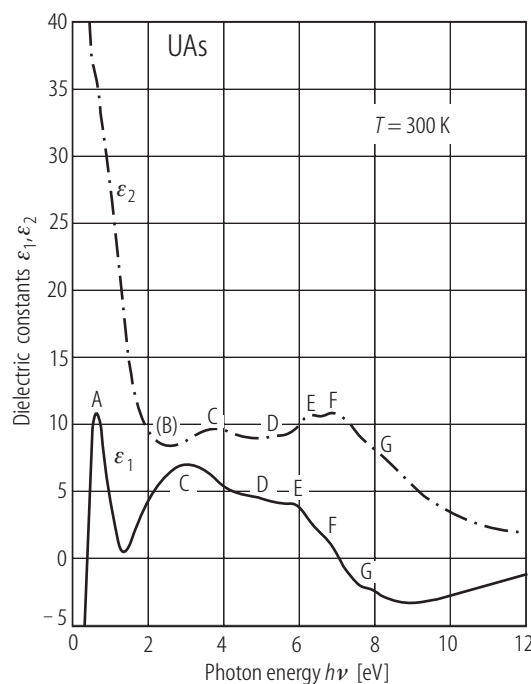


**Fig. IV.65.** UAs, USb s.c. Optical (NNIR) reflectivity,  $R$ , vs. photon energy,  $h\nu$ , for UAs and USb compared to that of CeN [80S3] and [84S1, 3]. Peaks A and B are assigned to the  $f \rightarrow d$  and  $d \rightarrow f$  transitions, respectively, while peak C corresponds to  $a(p,d) \Rightarrow f$  transition. The oscillator strength of the peak A for UAs and USb is similar to that in the uranium monochalcogenides. This similarity and the absence of any fine structure in those spectra, related to a final state splitting points to a substantial delocalization of the  $f$ -electrons. The main difference between CeN and the considered uranium mononictides is the absence of peak B in the optical spectrum of the latter compounds manifesting the small  $d$ -electron occupation in these materials.



**Fig. IV.66.** UAs, USb s.c. The real part of the optical conductivity,  $\text{Re } \sigma$ , as a function of photon energy,  $h\nu$ , [80S3]. In contrast to the uranium monochalcogenides, at low photon energies only one peak is observed. It follows from the fact of a much smaller number of conduction  $d$ -electrons than in uranium monochalcogenides, which makes any  $d \rightarrow f$  transition (peak B in Fig. IV.65) very weak. This does not allow to resolve the  $d \rightarrow f$  and  $f \rightarrow d$  peaks separately.



**Fig. IV.67.** UAs s.c. The real ( $\epsilon_1$ ) and imaginary ( $\epsilon_2$ ) parts of dielectric functions obtained by a Kramers-Kronig inversion vs. photon energy  $h\nu$  [80S3]. The sharp decreasing  $\epsilon_2$  with increasing energy indicates the conducting character of the compound. For both  $\epsilon_1$  and  $\epsilon_2$  there exist five further structures labeled from C to G, except for a sharp peak A and not distinctly marked peak B. For further discussion see the original paper and Fig. IV.65.

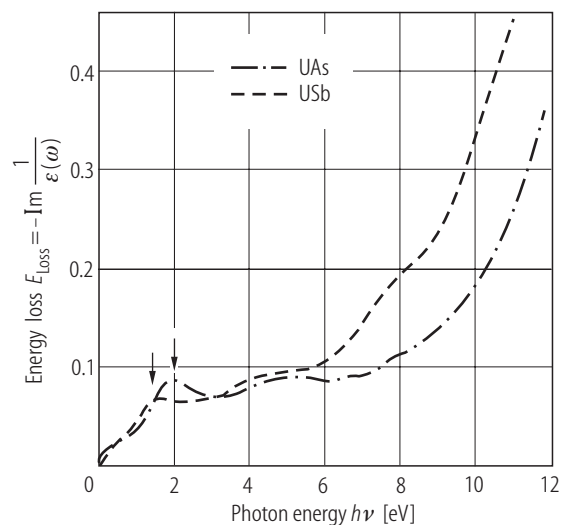


**Fig. IV.68.** UAs, USb s.c. The energy loss function  $E_{\text{loss}}$  vs. photon energy  $h\nu$ , in an energy range of small  $\epsilon_1$  and  $\epsilon_2$  - values as obtained from the reflectivity results (Fig. IV.67) [80S3]. Note that the collective excitations lead for both these mononitrides to rather small peaks, which are located at 2 eV and 1.6 eV (see arrows), respectively.

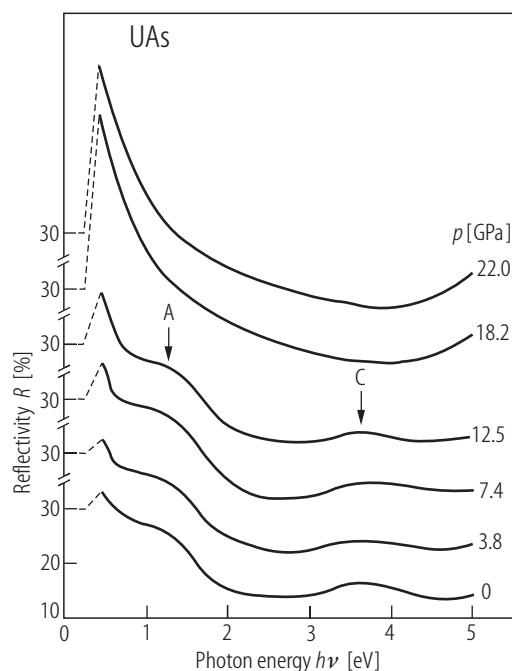


**Fig. IV.69.** UAs. Optical reflectivity,  $R$ , vs. photon energy  $h\nu$  under various pressures (indicated) [94B]. Note that all other curves than that at  $p = 0$  are shifted upward. The dashed lines indicate the corresponding reference value. The maxima A and C in reflectivity, observed around 1.2 and 3.5 eV, respectively, are characteristic of the B1 phase. They disappear at 18 GPa, i.e. at the transition pressure  $p_t$  into the B2 phase.

For Fig. IV.70 see next page

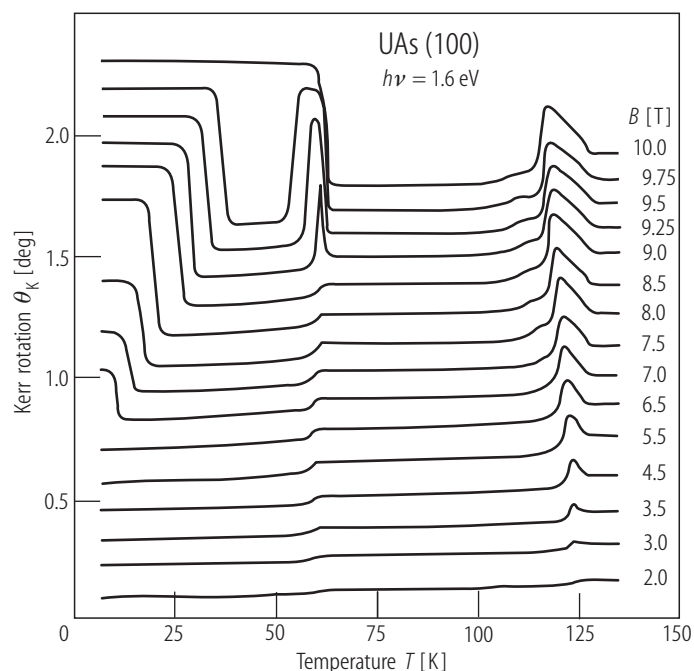


**Fig. IV.71.** UAs s.c. Kerr rotation,  $\theta_K$ , vs. temperature,  $T$ , measured on a cleaved single crystal in fields up to 10 T [84RSV]. For clarity the consecutive curves are shifted up by  $0.1^\circ$ . Note that around  $T_N$  ( $= 124.5$  K) an intermediate phase with a higher magnetization appears at medium fields. Neutrons identified it as a single- $k$  ferrimagnetic phase with a  $++-$  stacking of (001) ferromagnetic planes [82RBQV]. Furthermore, for  $B < 9$  T, at  $T_t = 62$  K the transition to the AF  $1A-2k$  structure is seen. In addition, between 53 and 62 K, at  $B > 9.2$  T one further magnetic structure is found being not identified by neutron diffraction.  $p_S = 0.53 \mu_B/\text{U atom}$ . This may correspond to the Ferri- $2k$  structure.

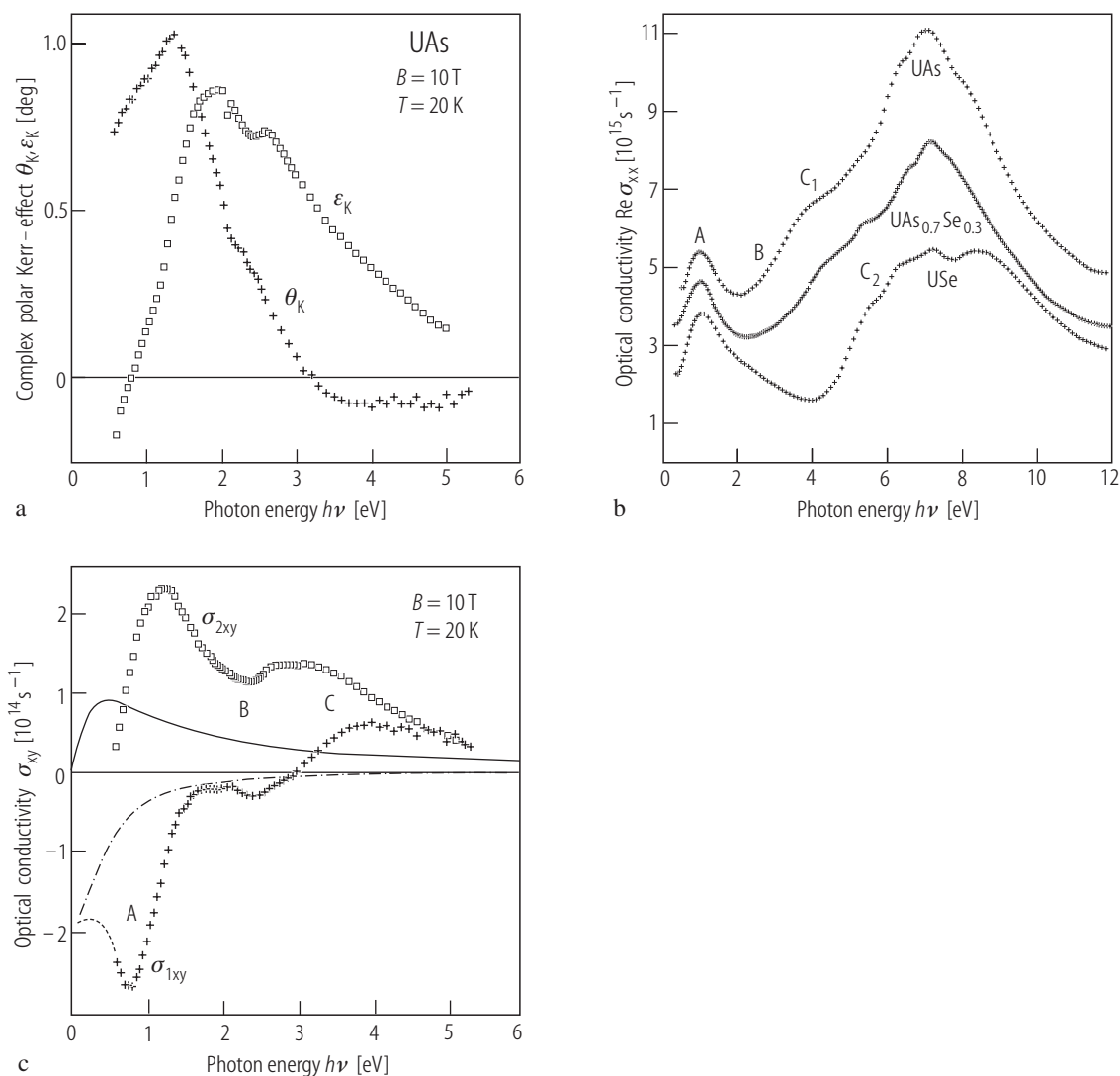


**Fig. IV.70.** UAs s.c. (a) Complex polar Kerr effect ( $\theta_K$  and  $\epsilon_K$  are Kerr-rotation and Kerr-ellipticity, respectively) of a (100) cleaved single crystal as a function of photon energy,  $h\nu$ , measured in the range from 0.5 to 5.7 eV at 20 K in 10 T [84RSV], [86R]. In an applied field of about 9 T, a ferromagnetic phase exists with  $p_S \approx 0.42 \mu_B$  [80VWB]. (b) Absorptive part of the diagonal conductivity,  $\text{Re } \sigma_{xx}$ , of UAs compared to that for  $\text{UAs}_{0.7}\text{Se}_{0.3}$  and USe taken at RT and  $B = 0$  [84RSV]. The curves are vertically shifted by one unit. Note that two strong interband transitions (peaks A and B) are seen at low photon energy, while the broad absorption bands around 7.5 eV showing structure are attributed to VB excitations (see [80S3]). (c) Absorptive ( $\sigma_{2xy}$ ) and dispersive ( $\sigma_{1xy}$ ) part of the off-diagonal conductivity as a function of photon energy,  $h\nu$ , at the

magnetic saturation ( $p_S = 0.42 \mu_B$  at 10 T and 20 K) [86R]. The dashed line for  $h\nu \leq 0.5$  eV is obtained by Kramers-Kronig relation between  $\sigma_{1xy}(\omega)$  and  $\sigma_{2xy}(\omega)$ . The solid and dashed-dot curves are estimated free-electron contributions to  $\sigma_{2xy}$  and  $\sigma_{1xy}$ , respectively. The positive sign in  $\sigma_{2xy}$  is equivalent to a negative conduction spin polarization. Peak A is assigned to a transition from a narrow f-band at  $E_F$  into d states (f→d transition). The absence of any fine structure in  $\sigma_{xy}$  points to an f-band width being larger than typical spin-orbit energies. Peak B at 2.3 eV may be interpreted in terms of a d→f transition, which appears in the case of not-localized f states. Peak C around 3 eV is interpreted as the onset of excitations from the top of the VB, i.e. as a (p,d)→f transition.

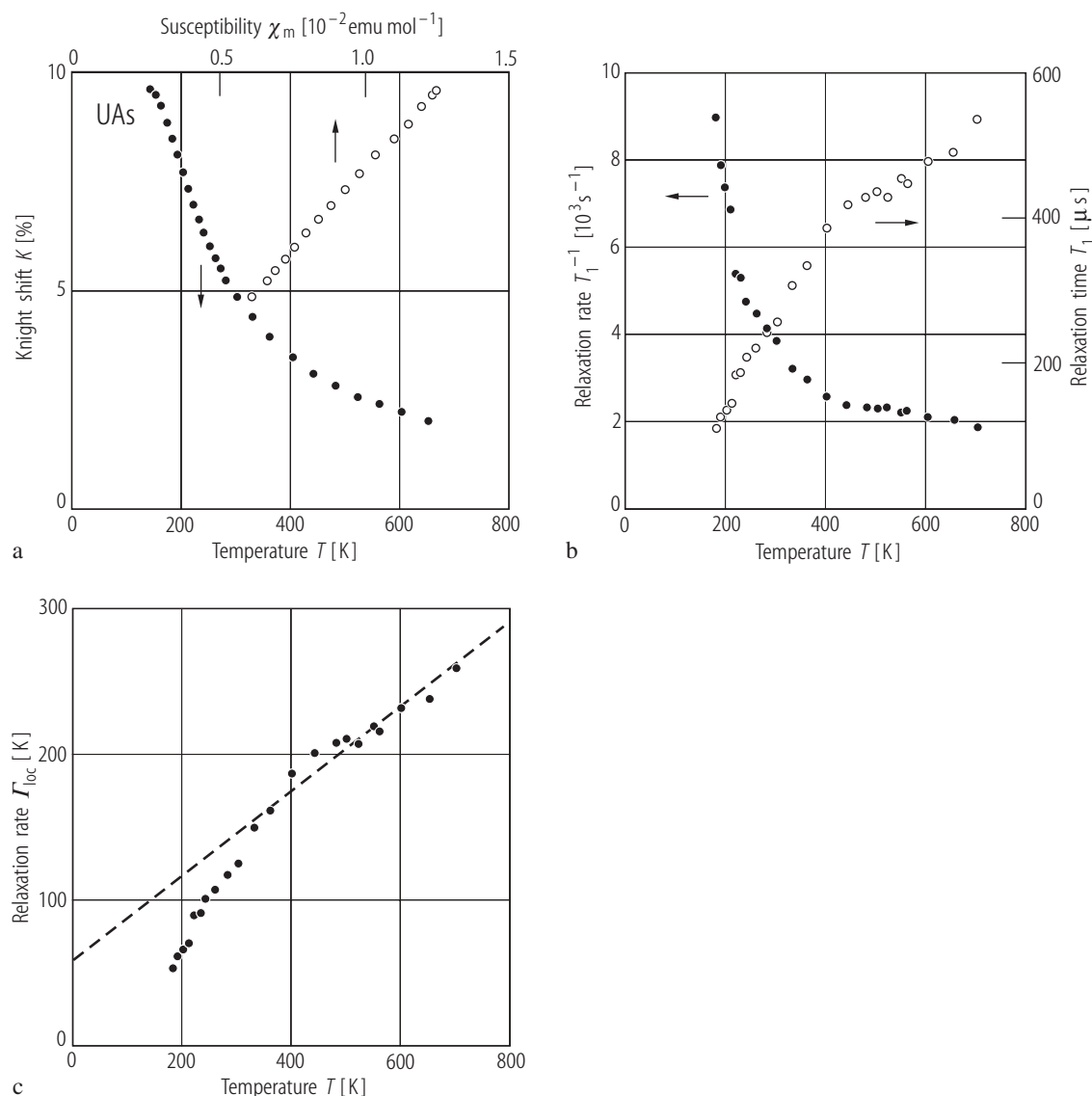


**Fig. IV.72.** UAs. **(a)** Knight shift,  $K$ , of the  $^{75}\text{As}$  NMR vs. molar susceptibility,  $\chi_m$ , (open circles) and vs. temperature,  $T$ , between 140 and 650 K (closed circles) [93STMV].  $A_{\text{hf}} = 41.8$  (kOe/ $\mu_B$ ) being twice as large as that for  $^{31}\text{P}$  in UP [67SGB]. **(b)** The relaxation,  $T_1$  (rhs) (open circles) and reverse relaxation,  $T_1^{-1}$ , (lhs) (closed circles) as a function of temperature,  $T$ , up to 700 K [93STMV]. Note a typical divergent behaviour of  $T^{-1}(T)$  on approaching  $T_N$ . Also neutron measurements [82LLMM] revealed diverging spin

fluctuations (SF) with  $Q = 2\pi/a$  (0,0,0.7) as  $T \rightarrow T_N$ , although the transition to AF I structure is of first order. **(c)** The relaxation rate of spin fluctuations  $\Gamma_{loc}$  as a function of temperature,  $T$ , [93STMV]. Above 300 K  $\Gamma_{loc} = 0.29T + 58.9$  [K] in terms of anisotropic THI. This compared to  $\Gamma_{loc}(T)$  of UP (see Fig. III.55) gives a larger intercept and smaller slope for UAs which indicates the relative importance of the exchange interaction increasing from UP to UAs.

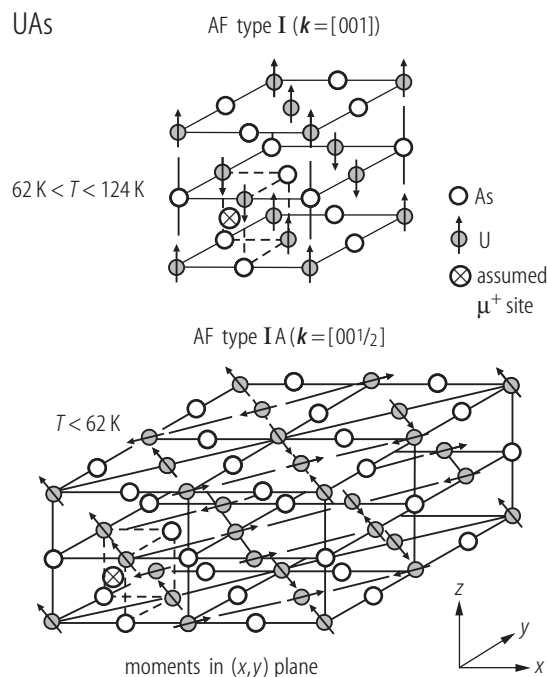


**Fig. IV.73.** UAs. Magnetic structures of AF I and a new AF IA-type, determined by [68LMT] which was not predicted by MFT, are characterized by wave vectors  $k$  and Fourier component  $m(k)$  parallel to  $k$ . The corresponding vectors  $k$  are  $[001]$  and  $[00\frac{1}{2}]$ , but the ordering is either collinear or multiaxial, respectively. The magnetic moments are then either along  $[100]$  in single- $k$  or along  $[110]$  in double- $k$  structure [80RBQV]. Moreover, there exist several symmetry equivalent  $k$  vectors that give rise to the existence of several magnetic domains. In addition, the single- $k$  (top) and double- $k$  (bottom) structures have a tetragonal symmetry with the magnetic moments parallel and perpendicular to the tetragonal axis, respectively. The first transition at  $T_N$  requires a tetragonal distortion with  $c/a < 1$  while the second one at  $T_t$  with  $c/a > 1$ . Only the latter has been detected in RXMS experiment [90MVII]. The crossed circle symbol gives a probable site for the muon  $\mu^+$  in the center of the uranium tetrahedron in both types of magnetic structures [86ABGK].

For Fig. IV.74 see next page

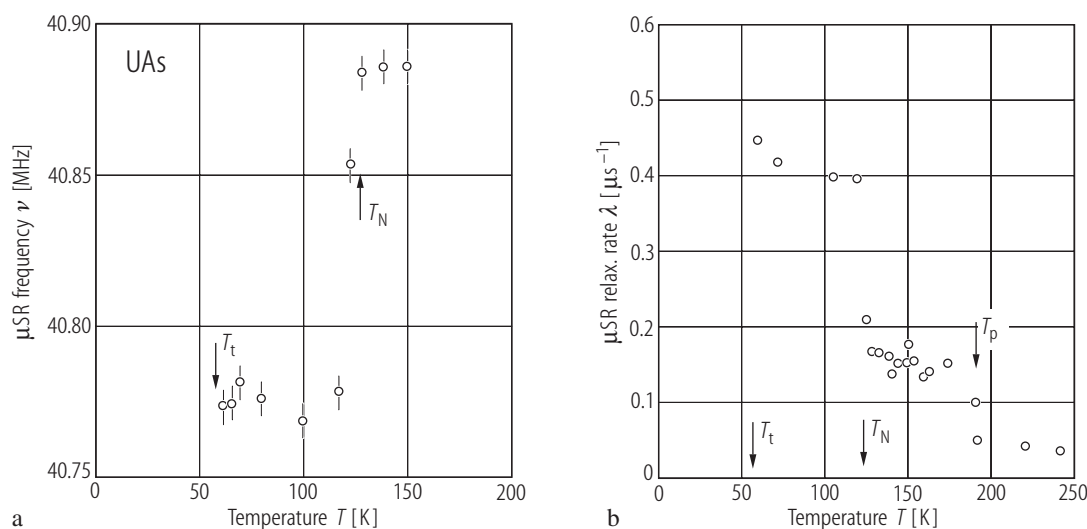


**Fig. IV.75.** UAs. (a) The  $\mu^+$  spin rotation frequency,  $\nu$ , and (b) relaxation rate,  $\lambda$ , in TF at 300 mT, as a function of temperature [86ABGK]. The behaviour between 190 K and  $T_N$  is treated as an indicator of the formation of the magnetic precursor phase (see [81SLSV]). See also that at  $T_N$  (=124 K)

$\lambda$  jumps abruptly due to a first-order magnetic phase transition. Another  $\lambda$  jump is expected at  $T_t = 62$  K. However the complex spectra taken within the stability of AF IA- $2k$  magnetic structure do not allow determining a single value of  $\lambda$  (see also [87ABGK] and [89A]).

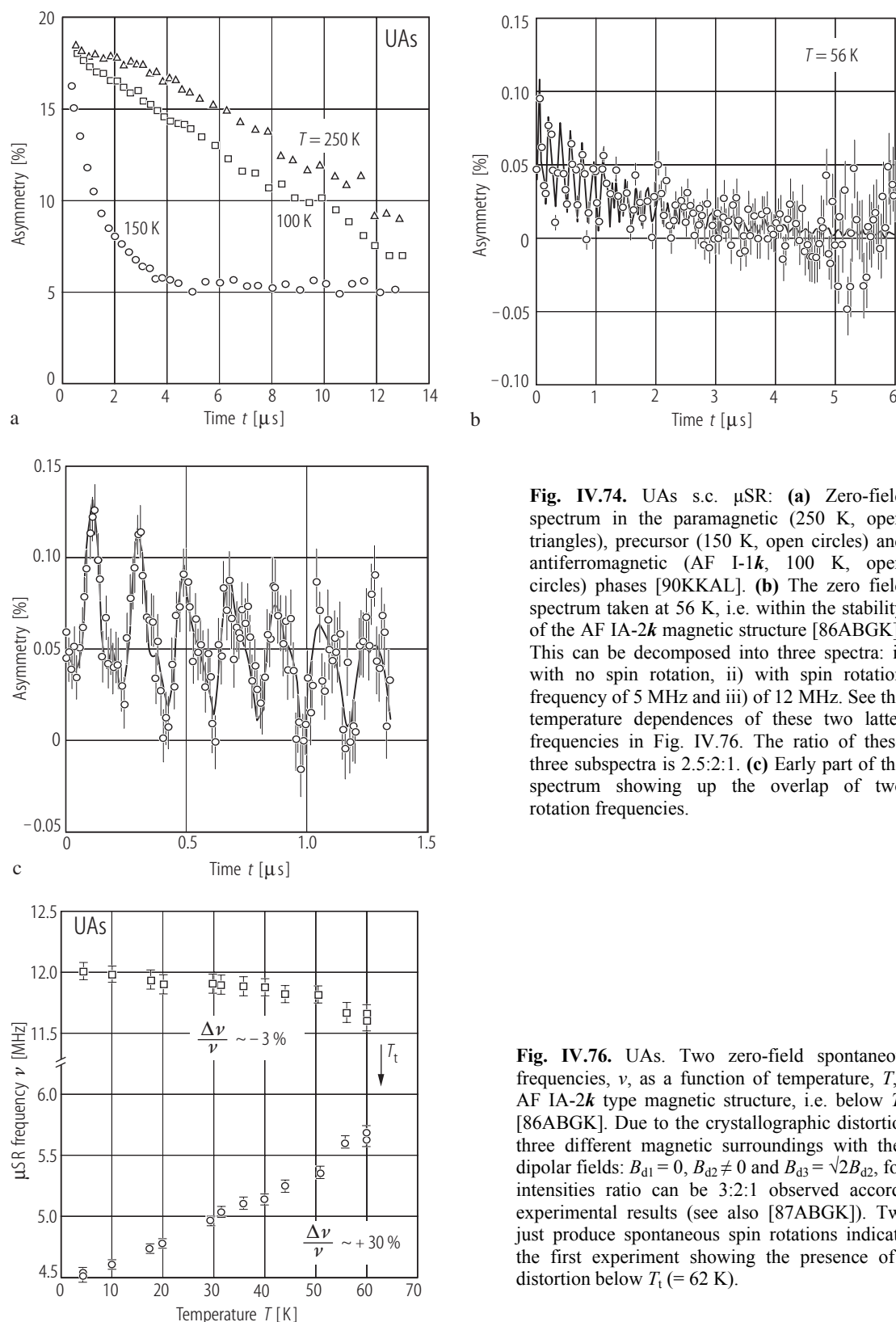


**Fig. IV.74.** UAs s.c.  $\mu$ SR: **(a)** Zero-field spectrum in the paramagnetic (250 K, open triangles), precursor (150 K, open circles) and antiferromagnetic (AF I-1 $k$ , 100 K, open circles) phases [90KKAL]. **(b)** The zero field spectrum taken at 56 K, i.e. within the stability of the AF IA-2 $k$  magnetic structure [86ABGK]. This can be decomposed into three spectra: i) with no spin rotation, ii) with spin rotation frequency of 5 MHz and iii) of 12 MHz. See the temperature dependences of these two latter frequencies in Fig. IV.76. The ratio of these three subspectra is 2.5:2:1. **(c)** Early part of the spectrum showing up the overlap of two rotation frequencies.

**Fig. IV.76.** UAs. Two zero-field spontaneous rotation frequencies,  $\nu$ , as a function of temperature,  $T$ , within the AF IA-2 $k$  type magnetic structure, i.e. below  $T_t$  ( $= 62$  K) [86ABGK]. Due to the crystallographic distortion there are three different magnetic surroundings with the following dipolar fields:  $B_{d1} = 0$ ,  $B_{d2} \neq 0$  and  $B_{d3} = \sqrt{2}B_{d2}$ , for which the intensities ratio can be 3:2:1 observed according to the experimental results (see also [87ABGK]). Two of these just produce spontaneous spin rotations indicated. This is the first experiment showing the presence of the lattice distortion below  $T_t$  ( $= 62$  K).

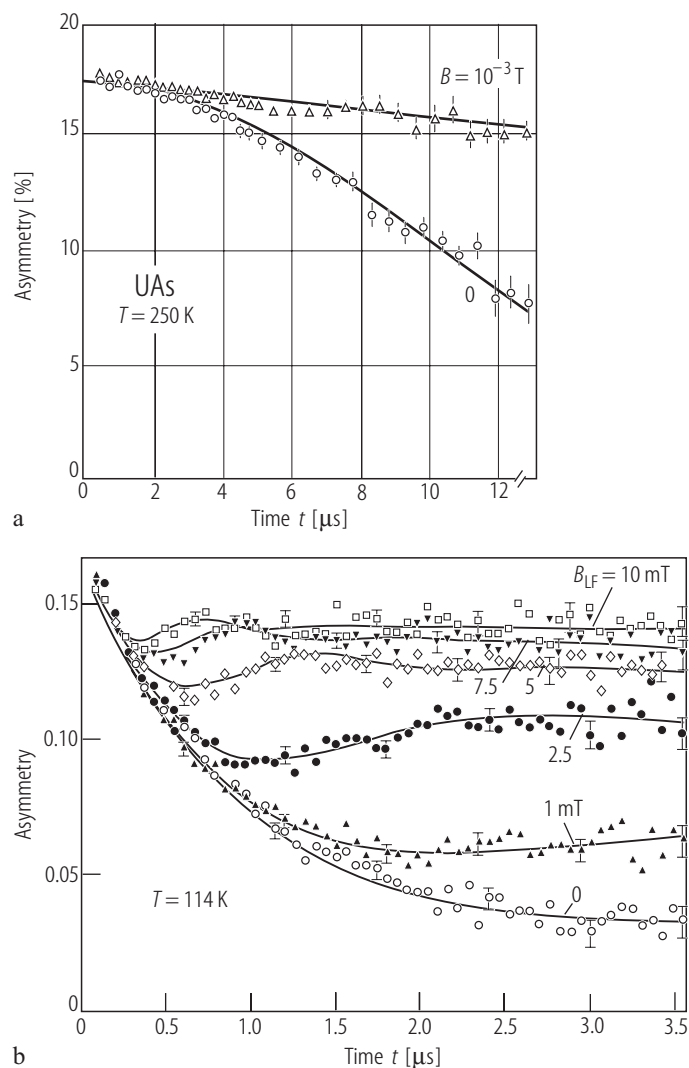


**Fig. IV.77.** UAs. Longitudinal field (LF) decoupling  $\mu$ SR spectra taken at: **(a)** 250 K (paramagnetic phase) and **(b)** 114 K (within the AF I- $1k$  phase) taken at different magnetic fields: 0 (open circles), 1 mT (closed triangles up), 2.5 mT (closed circles), 5 mT (open diamonds), 7.5 mT (closed triangles down) and 10 mT (open squares) [90KKAL]. Note that the field of 1 mT fully decouples the nuclear depolarization in the paramagnetic state (static muon), and the weak exponential decay, which remains for  $B_{LF} > 10$  mT (figure **(b)**) arises from fast fluctuating ( $1/\tau = 10^{13}$  Hz) atomic moments on uranium. In the AF I- $1k$  phase no spontaneous rotation is observed in zero field.

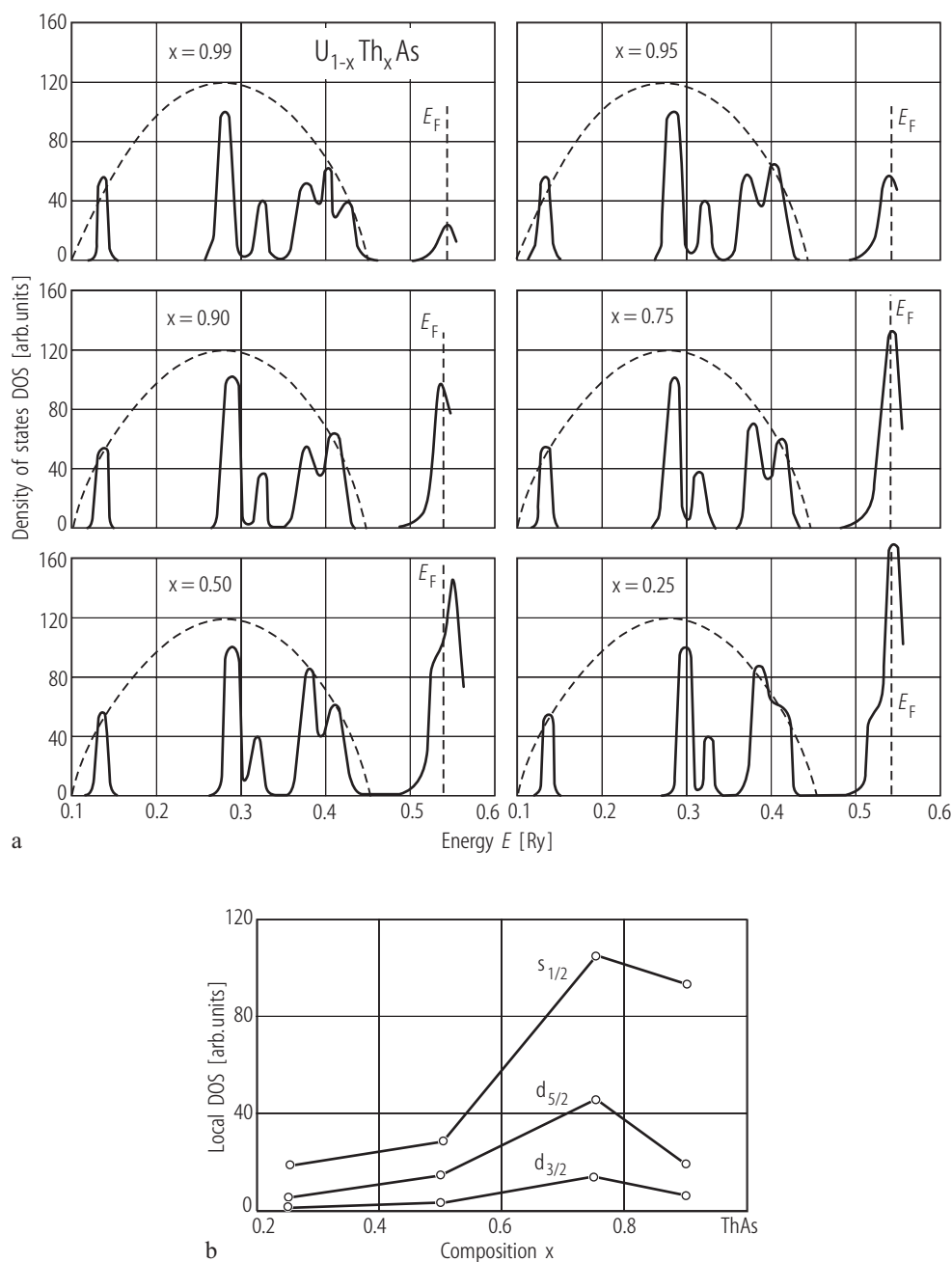


**Fig. IV.78.** (U,Th)As. **(a)** The occupied part of the DOS for the solid solutions  $U_{1-x}Th_xAs$  with  $x = 0.25, 0.50, 0.75, 0.90, 0.95$  and  $0.99$  [80 WP]. The dashed line indicates a broad peak of the "As-p" band expected in this energy region. One sees that the peak at  $E_F$  is substantially

increased with decreasing molar fraction  $x$  ( $E_F$  is almost constant). The data can be related to XPS experiment. **(b)** Local DOS of the  $s_{1/2}$ ,  $d_{3/2}$  and  $d_{5/2}$  states for the non-metal (As) in the vicinity of the Fermi energy, as a function of the concentration  $x$  [80WP].



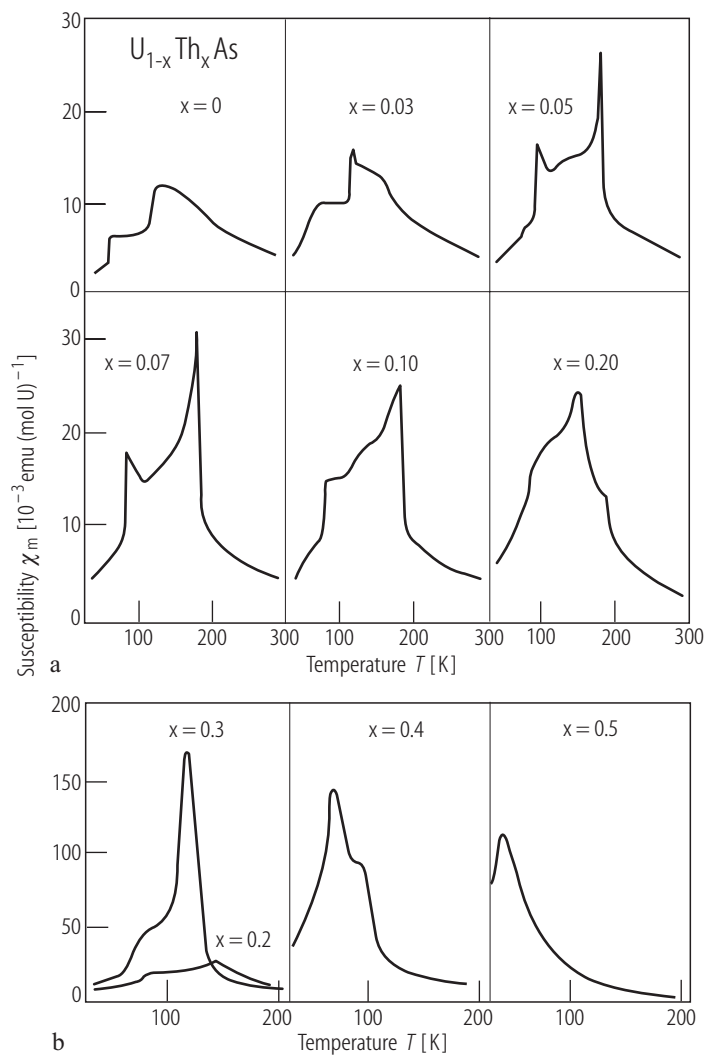


**Fig. IV.79.** (U,Th)As s.c. Molar magnetic susceptibility,  $\chi_m$  vs. temperature,  $T$ , for the solid solutions  $U_{1-x}Th_xAs$  having low thorium concentration: **(a)**  $x \leq 0.2$  [84BBTV] and **(b)**  $0.3 \leq x \leq 0.5$ . Note that the progressive substitution of uranium by thorium causes a complex shape of  $\chi_m(T)$  with a number of anomalies characteristic of phase transitions (see non-shaded part of  $(T, x)$  MPD in Fig. IV.80). Except for the well known magnetic transitions (see [80FSV]) there are probably new ones (shaded part). The existence of susceptibility anomalies above the ordering temperatures is confirmed by the occurrence of inflection points in isofield (8 T) thermal magnetization (not shown), caused probably by a short-range order or an incommensurate magnetic phase. The contribution of the additional conduction electrons supplied by Th-substitution may be responsible for such behaviour.

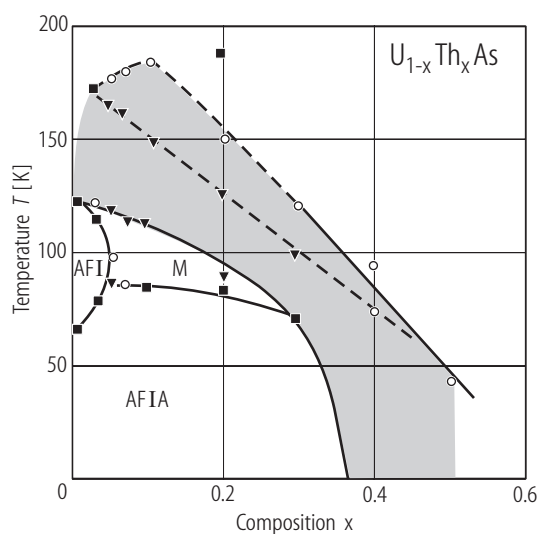


**Fig. IV.80.** (U,Th)As s.c.  $(T,x)$  MPD for the  $U_{1-x}Th_xAs$  solid solutions [84BBTV] determined by  $\chi_{ac}$  measurements. M denotes a sine-modulated magnetic phase [80FSV]. The shaded part of diagram is discussed in Fig. IV.79.

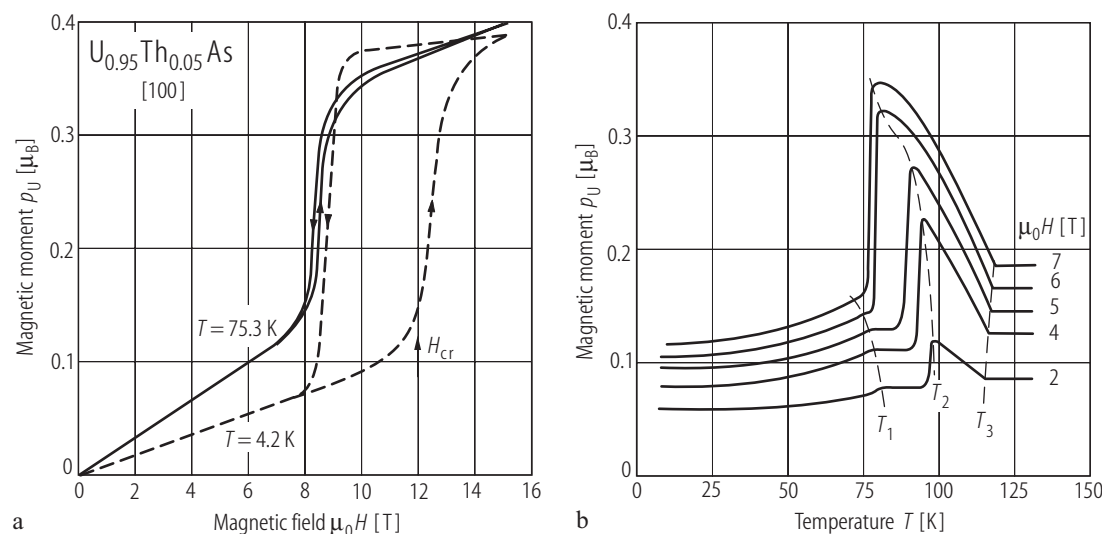


**Fig. IV.81.** (U,Th)As s.c. **(a)** Magnetic moment per U atom,  $p_U$ , of the solid solution  $U_{0.95}Th_{0.05}As$  vs magnetic field,  $H$ , applied along the [100] direction up to 15 T and taken at two temperatures indicated [80V]. Note the onset of a new ferromagnetic structure above  $\mu_0 H_{cr} = 12$  T at 4.2 K. The saturation moment  $p_s$  is only one-third of the full moment of  $p_U$  at 15 T. Hysteresis is large at 4.2 K and vanishes

rapidly with increasing temperature. **(b)** Magnetic moment  $p_U$ , for the same composition vs. temperature,  $T$ , measured along the [100] direction in applied magnetic fields from 2 to 7 T [80V]. Note three different critical temperatures  $T_1 = T_i$  (AFIA  $\rightarrow$  AFI),  $T_2 = T_{IC}$  (AFI  $\rightarrow$  LSW) and  $T_3 = T_N$  (LSW  $\rightarrow$  Para).

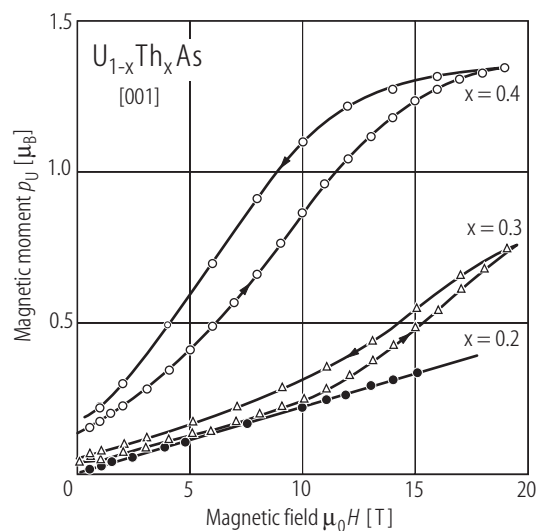


**Fig. IV.82.** (U,Th)As s.c. Magnetic moment,  $p_U$ , at 4.2 K vs. magnetic field,  $H$ , up to 19 T applied along the [001] direction for the solid solutions  $U_{1-x}Th_xAs$  with  $x$  indicated [84BBTV]. Note that for  $x > 0.2$  a metamagnetic phase transition is apparent.

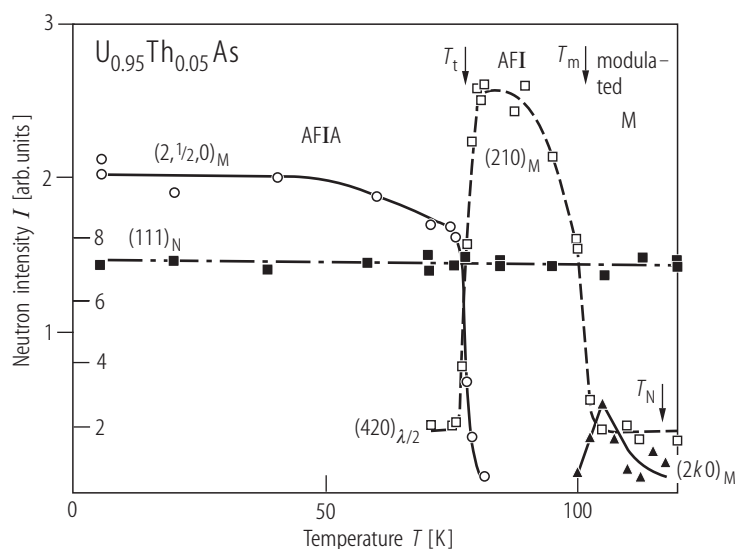
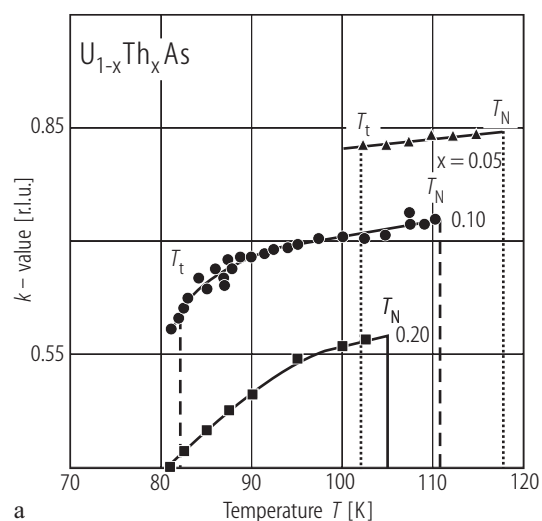
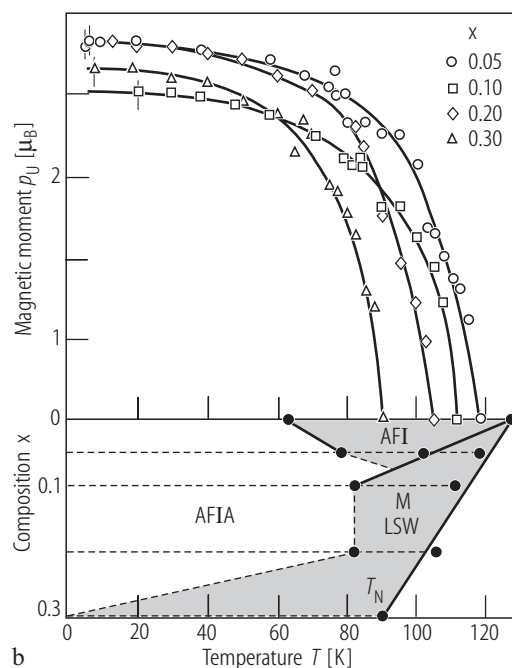


**Fig. IV.83.** (U,Th)As s.c. Neutron integrated intensities of  $(1,1,1)_N$ ,  $(2,0.5,0)_M$ ,  $(2,1,0)_M$  and  $(2,k,0)_M$  measured for  $\text{U}_{0.95}\text{Th}_{0.05}\text{As}$  as a function of temperature,  $T$ , [80FSV]. The constant intensity of the nuclear  $(1,1,1)_N$  peak proves anti-ferromagnetism. Note three transitions at  $T_t$ ,  $T_m$  and  $T_N$  from AF IA  $\rightarrow$  AF I  $\rightarrow$  LSW  $\rightarrow$  Para, respectively.



a



b

**Fig. IV.84.** (U,Th)As s.c. (a) The temperature dependence of  $k$ -values, corresponding to sinusoidally modulated phase LSW (reflection  $(2, k, 0)$ ) in the solid solutions  $\text{U}_{1-x}\text{Th}_x\text{As}$  for  $x = 0.05, 0.10$  and  $0.20$  determined between  $T_t$  and  $T_N$ . A constant value of  $k$  ( $= 0.469(2) \approx 8/17$ ) is reported for  $x = 0.3$  at all temperatures below  $T_N$  [80FSV]. (b) Ordered magnetic moment,  $p_U$ , determined for several

compositions  $x = 0.05$  (open circles),  $0.10$  (open squares),  $0.20$  (open diamonds) and  $0.30$  (open triangles) as a function of temperature,  $T$ , [80FSV]. The lower section presents the  $(T, x)$  MPD of this system (compare the MPD determined by bulk magnetic measurements for  $x \leq 0.10$  by [80VB]).

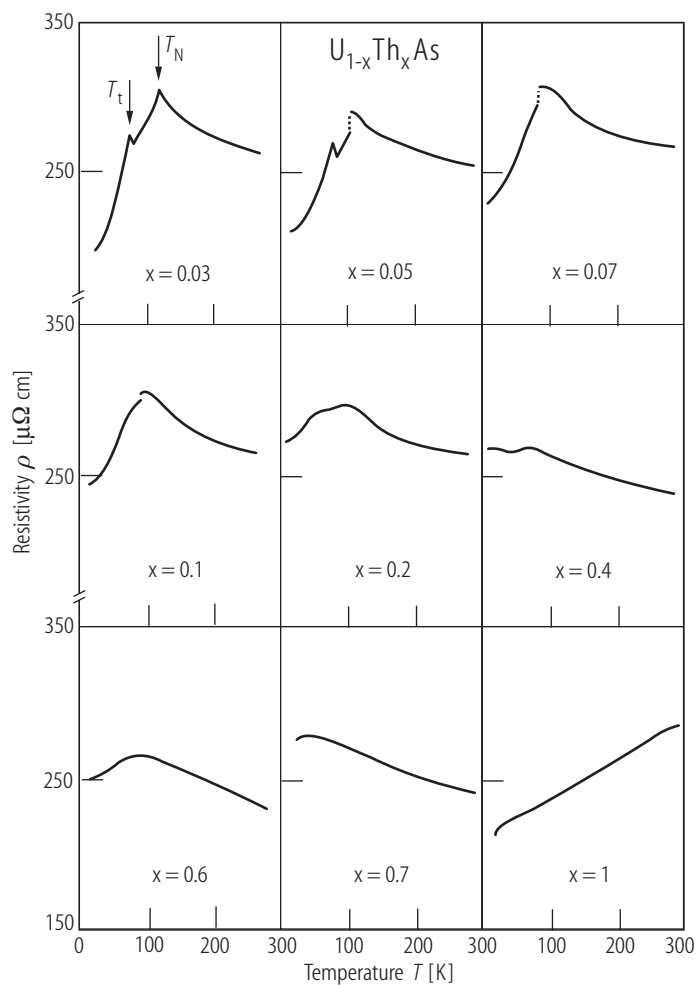
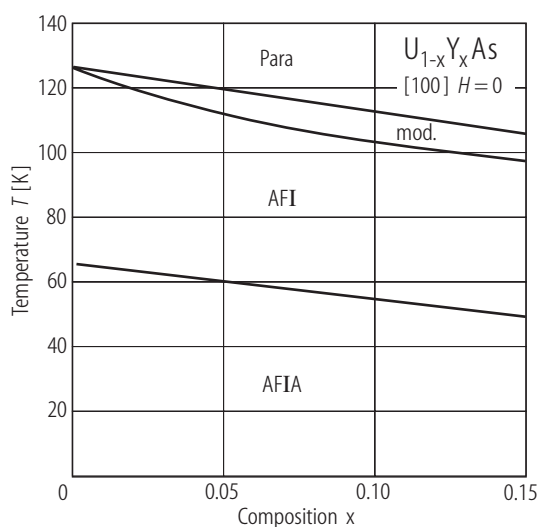
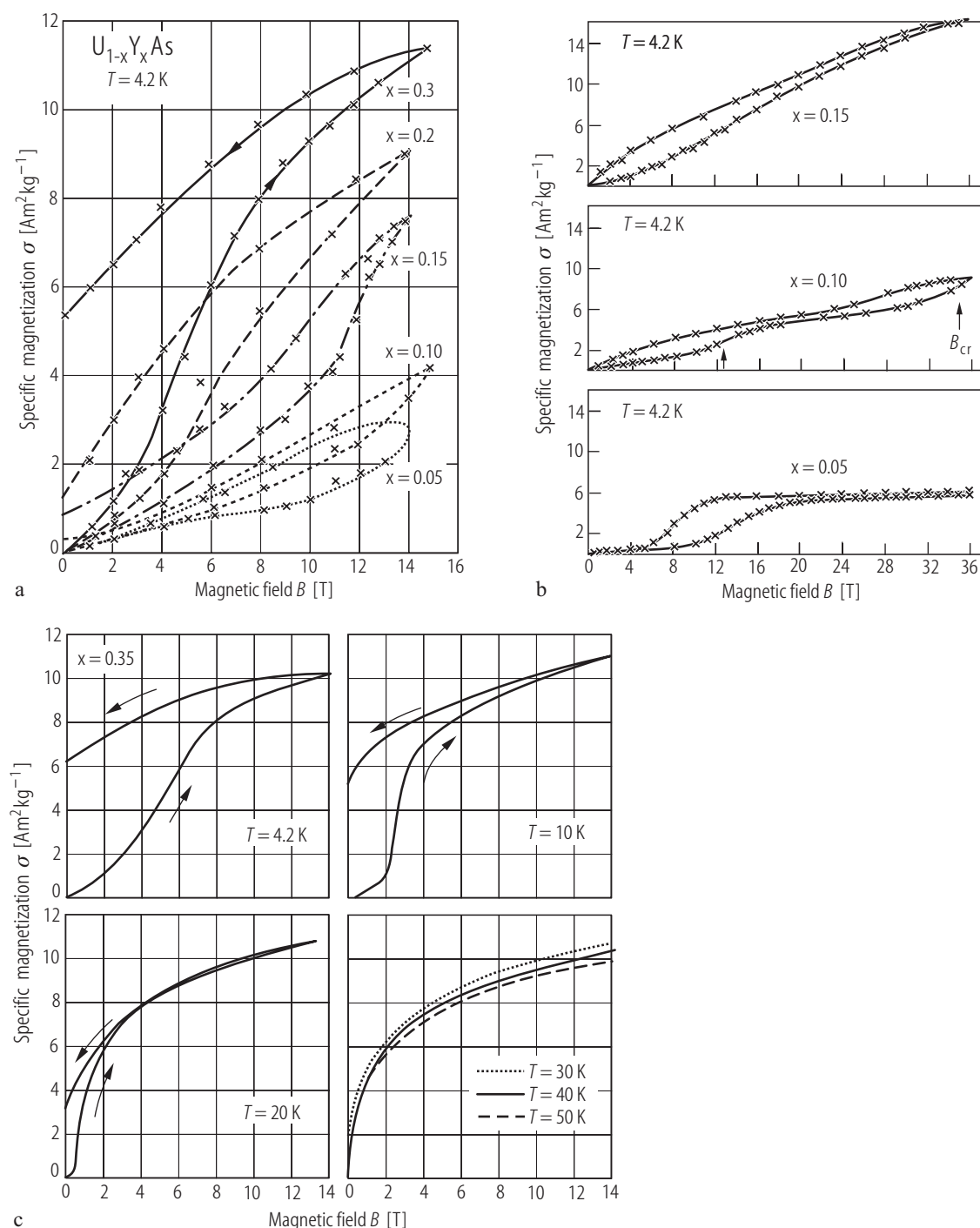


**Fig. IV.85.** (U,Th)As. Electrical resistivity,  $\rho$ , vs. temperature,  $T$ , for the solid solutions  $U_{1-x}Th_xAs$  with  $x$  indicated [94NBBB]. Note that negative sign of  $d\rho(T)/dT$  at  $T > T_N$  is preserved at least up to  $x = 0.7$ .



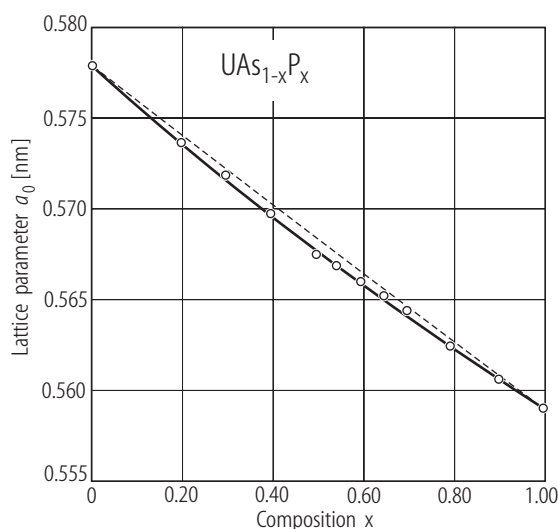
For Fig. IV.86 see next page

**Fig. IV.87.** (U,Y)As s.c. ( $T$ ,  $x$ ) MPD of the solid solutions  $U_{1-x}Y_xAs$  for  $x \leq 0.15$  [83CTV]. The effect of dilution of magnetic exchange is observed only. Compare it with the corresponding diagram of (U, Th)As presented in Fig. IV.84.

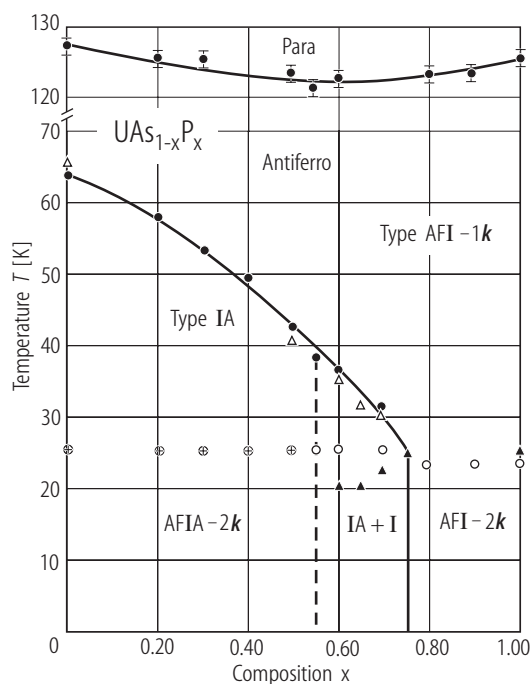


**Fig. IV.86.** (U,Y)As. (a) Specific magnetization,  $\sigma$ , (in  $\text{Am}^2/\text{kg}$  units) vs. magnetic field,  $B$ , up to 14 T and at 4.2 K for the solid solutions  $\text{U}_{1-x}\text{Y}_x\text{As}$  for  $0.05 \leq x \leq 0.3$  [89PM]. Note a change of AF ordering to a probably ferrimagnetic one as in the case of pure UAs, but with a rapid decrease of  $B_{cr}$  with increasing Y content  $x$ . (b) A plot of  $\sigma$  vs.  $B$  up to 36 T at 4.2 K obtained in pulsed fields for  $x = 0.05, 0.10$  and  $0.15$  [89PM]. Note for  $x = 0.1$  the existence of the

second critical field near 30 T. (c) Plots of  $\sigma$  vs.  $B$  taken up to 14 T at several temperatures from 4.2 to 50 K for  $\text{U}_{0.65}\text{Y}_{0.35}\text{As}$  [89PM]. There is an apparent vanishing of the hysteresis in  $\sigma(B)$  runs and decreasing  $B_{cr}$  with increasing temperature. As is indicated in [85P],  $T_C$  for the compositions  $0.2 \leq x \leq 0.45$  is nearly constant with a value of around 63(3) K.

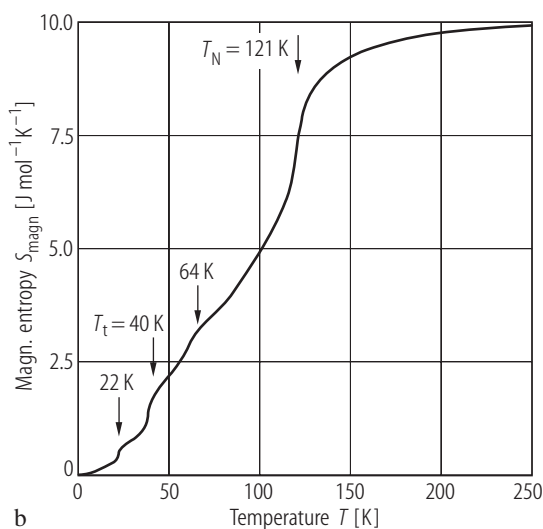
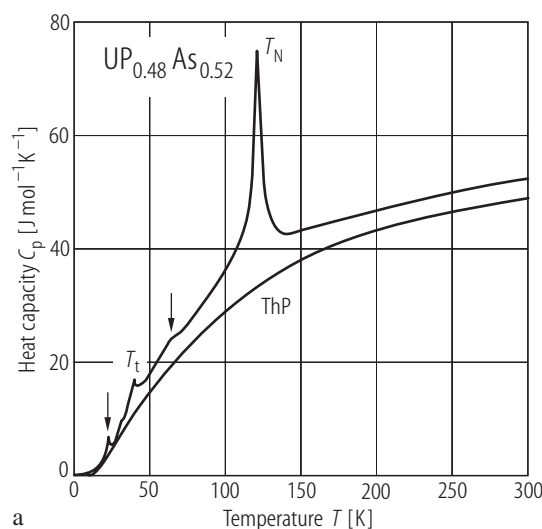


**Fig. IV.88.** U(P,As). Lattice parameter,  $a_0$ , vs. the P composition in the solid solutions  $\text{UAs}_{1-x}\text{P}_x$  [74T].



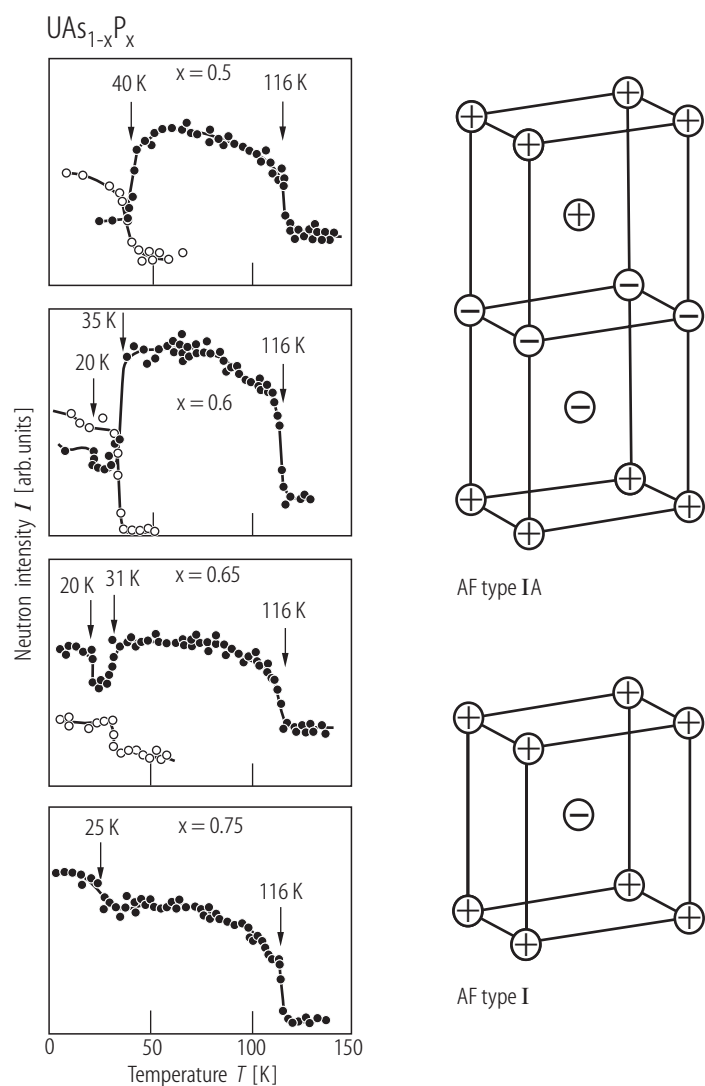
**Fig. IV.89.** U(As,P). Magnetic phase diagram,  $(T, x)$  MPD, for the solid solutions  $\text{UAs}_{1-x}\text{P}_x$  [74T]. Note some composition region of coexistence of the magnetic phases IA and I, confirmed by neutron diffraction [71LMP]. Open and closed triangles are neutron diffraction results, closed and open circles are the results based on the susceptibility measurements, respectively. Circles with crosses indicate the presence of a small anomaly in  $\chi(T)$ .

For Fig. IV.90 see next page

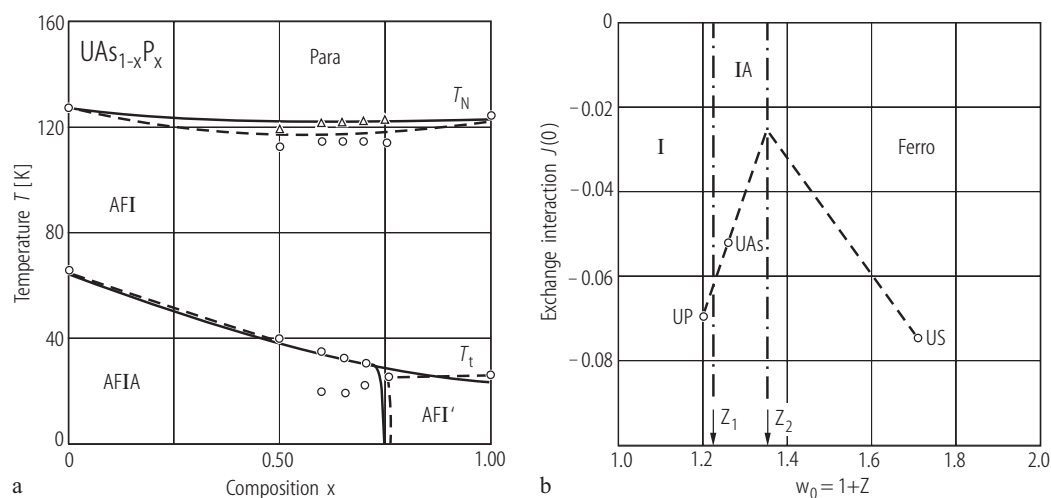


**Fig. IV.91.** U(As,P). **(a)** Heat capacity  $C_p$  vs. temperature,  $T$ , for  $\text{UAs}_{0.52}\text{P}_{0.48}$  compared to that of ThP [85BLGT]. This composition is close to the region of coexistence of two magnetic phases AF IA and AF I – the arrows show traces of the latter. The transition temperatures  $T_t$  (= 40 K) and  $T_N$

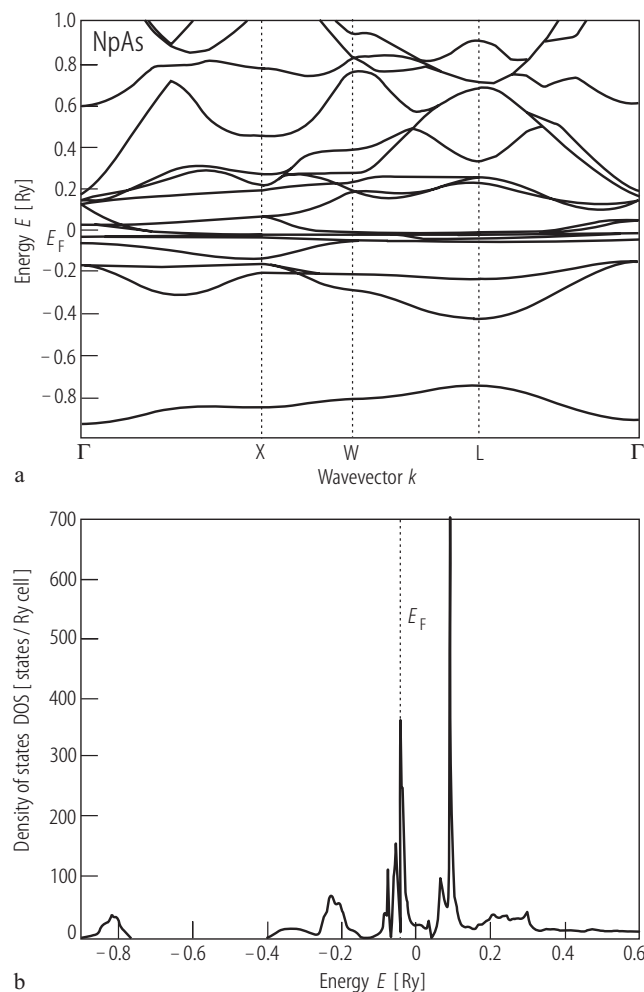
(= 121 K) correspond to those found from the magnetic susceptibility [74T] and neutron diffraction [71LMP] investigations. **(b)** Magnetic entropy,  $S_{\text{magn}}$ , vs. temperature,  $T$ , for  $\text{UAs}_{0.52}\text{P}_{0.48}$  [85BLGT]. For low-temperature anomalies see figure (a).



**Fig. IV.90.**  $\text{U}(\text{As},\text{P})$ . Neutron intensity  $I$  vs. temperature  $T$  for several compositions (indicated) of solid solutions  $\text{UAs}_{1-x}\text{P}_x$  [71LMP]. Closed circles show the changes in the AF-I phase, while open circles in the AF-IA phase.

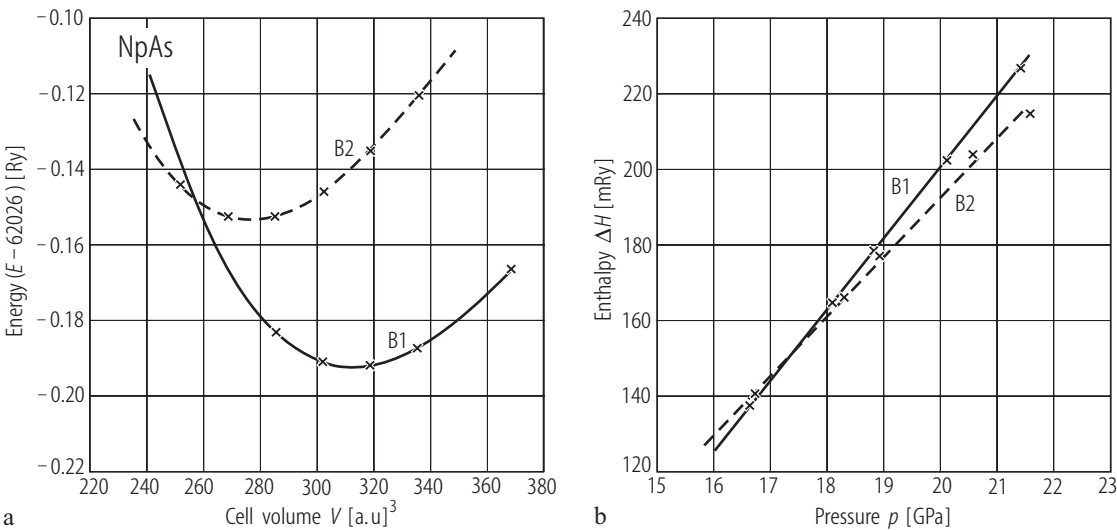


**Fig. IV.92.**  $U(As,P)$ . **(a)**  $(T,x)$  MPD of  $UAs_{1-x}P_x$  from [71LMP] (shown as dashed line together with open circles and triangles) compared to the theoretical one (solid lines) determined in terms of the electron-delocalization model (see Fig. R.13a) [74RE]. **(b)** Variation of the exchange interaction  $J(0)$  with the number of the band electrons  $w_0 (= 1+Z)$  per U ion at  $T = 0$  K [74RE]. Open circles are  $J(0)$  values deduced from the electron-delocalization theory [73RE].  $J(0)$  is given here in units of  $E_0$ , the Fermi level of the band when occupied by one electron per actinide ion. For the values in eV units see the paper and Table I there. See the critical values of  $Z$  separating the AF I and AF IA ferromagnetic phases.



**Fig. IV.93.** NpAs. Spin-polarized band structure calculated by TB LMTO within ASA at ambient pressure for the  $f^4d^1s^2$  configuration of Np [98TRN]. **(a)** “Spin-down” electron dispersion curves for NpAs in the B1 phase. The bands for the “spin-up” case are similar. The lowest lying bands are 4s states of As, and the bands in the valence region, just below  $E_F$ , are from the 4p states of As. Around  $E_F$  there are hybridized 5f-6d bands. **(b)** A histogram of the total DOS in the B1 phase at ambient pressure. Note a sharp peak due to 5f-electrons around 0.1 Ry in the valence region and a broad feature of 6d-electrons at about 0.2 Ry.

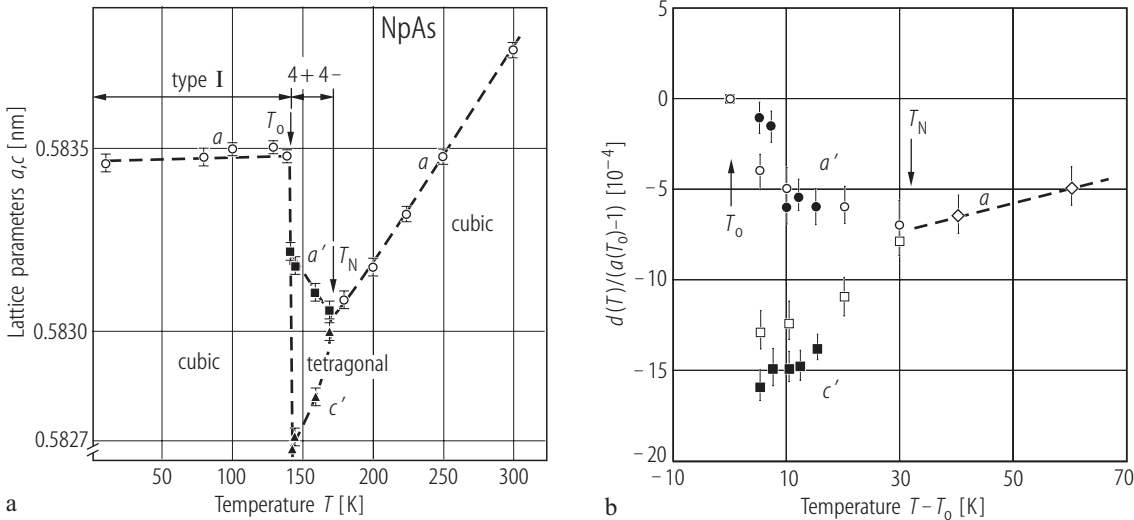




**Fig. IV.94.** NpAs. **(a)** The total energies calculated for different cell volumes,  $V$ , of the B1 and B2 phases, fitted to the Birch equation of state and **(b)** calculated enthalpy,  $\Delta H$ , vs. pressure,  $p$ , for the B1 and B2 phases [98TRN]. For the characteristic parameters compared to experiment see the Table.

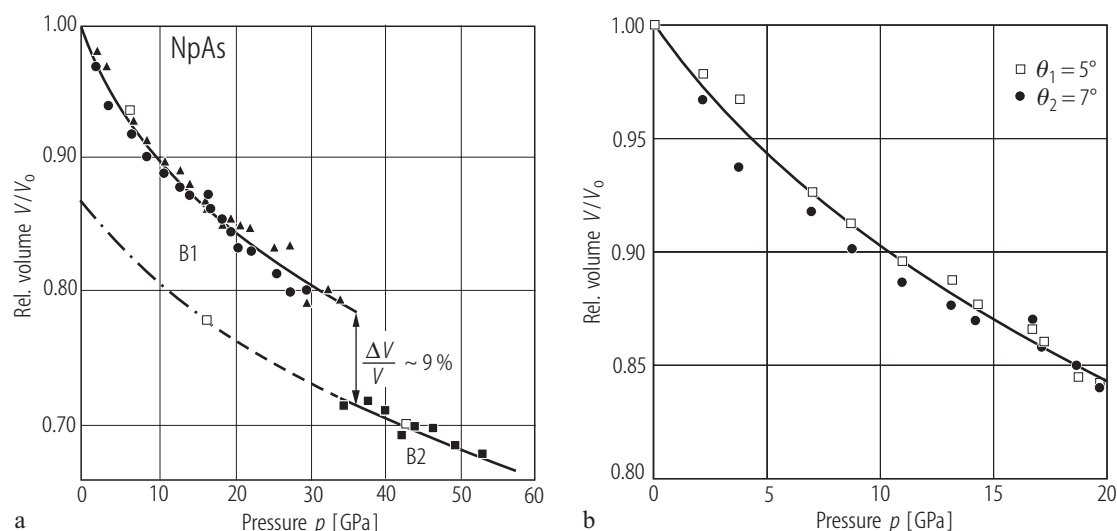
**Table:** Characteristic parameters for the B1 to B2 transition in NpAs induced by pressure.

Parameter	Calculation	Experiment
$p_t$ [GPa]	19.8	26
$\Delta V/V_0$ [%]	11.37	9
$B_0$ [GPa]	71.78	70.0
$a_0$ [nm]		
a) B1 phase	0.57026	0.58366
b) B2 phase	0.34402	0.3310



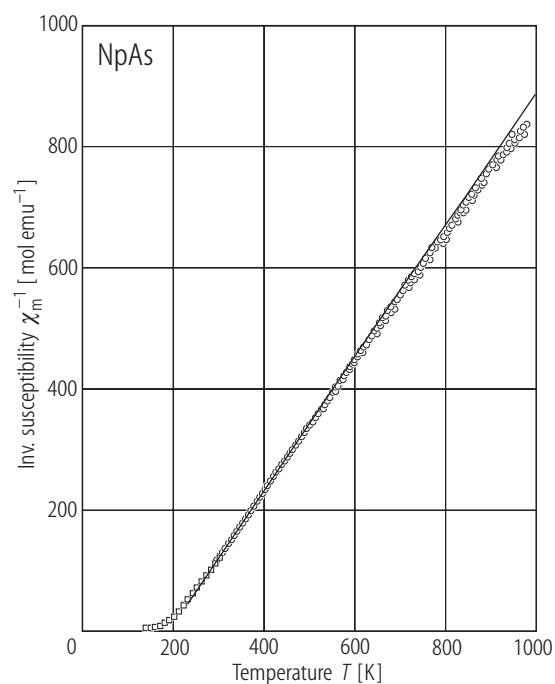
**Fig. IV.95.** NpAs. **(a)** Lattice parameters,  $a$ ,  $c$ , vs. temperature,  $T$ , [74ADHL]. This system is unique due to the lattice transition from cubic to tetragonal and again to cubic symmetry as the temperature is lowered. A discontinuity in the volume of the unit cell was observed at  $T_0 = 143$  K (see also Fig. R.45). No distortion occurs below  $T_0$  down to the quantity  $[(c - a)/a] \leq 3 \cdot 10^{-4}$ . (See also LB III/12c, p.435,

Fig.67). **(b)** Relative lattice parameters  $d$  (i.e.  $a$  or  $c$ ) normalized to  $a$  (at  $T_0$ ), as measured by RXMS using L and K scans through the (002) and (004) Bragg peaks as a function of temperature (closed symbols) compared to those of X-ray results (plot (a)) represented by open symbols [94LSLR2].



**Fig. IV.96.** NpAs. **(a)** Relative volume,  $V/V_0$ , vs. pressure,  $p$ , up to 53 GPa [86DDBS].  $a_0 = 0.5366(5)$  nm. Closed points are for increasing and open for decreasing applied pressures. The data were taken with use of a double conical slit allowing simultaneous use of two Bragg angles:  $\theta_1 = 5^\circ$  (triangles and squares) and  $\theta_2 = 7^\circ$  (circles). Such a technique increases the range of available  $d$ -values. Note good agreement between two sets of data. The compound undergoes a phase transformation B1→B2 which starts

around 25 GPa and is completed at 40 GPa. On pressure decrease, hysteresis to transformation lasts down to 16 GPa (open square). The 9% volume decrease of the phase transition at 37 GPa is consistent with the increase in the CN from 6 to 8. **(b)** The pressure-volume data for both diffraction angles within the B1 phase up to 20 GPa, for which the Birch and Murnaghan equations were fitted (both equations follow the solid line).  $B_0 = 70(1)$  GPa,  $B_0' = 6.2(4)$ . See also Table 6 [86DDBS].



**Fig. IV.97.** NpAs s.c. Inverse molar magnetic susceptibility,  $\chi_m^{-1}$ , vs. temperature,  $T$ , measured up to 980 K [98VMLR].  $\Theta_p = 190$  K,  $p_{\text{eff}} = 2.67 \mu_B$  and  $\chi_0 = 25 \cdot 10^{-6}$  emu/mol. The straight line is the Curie-Weiss law.

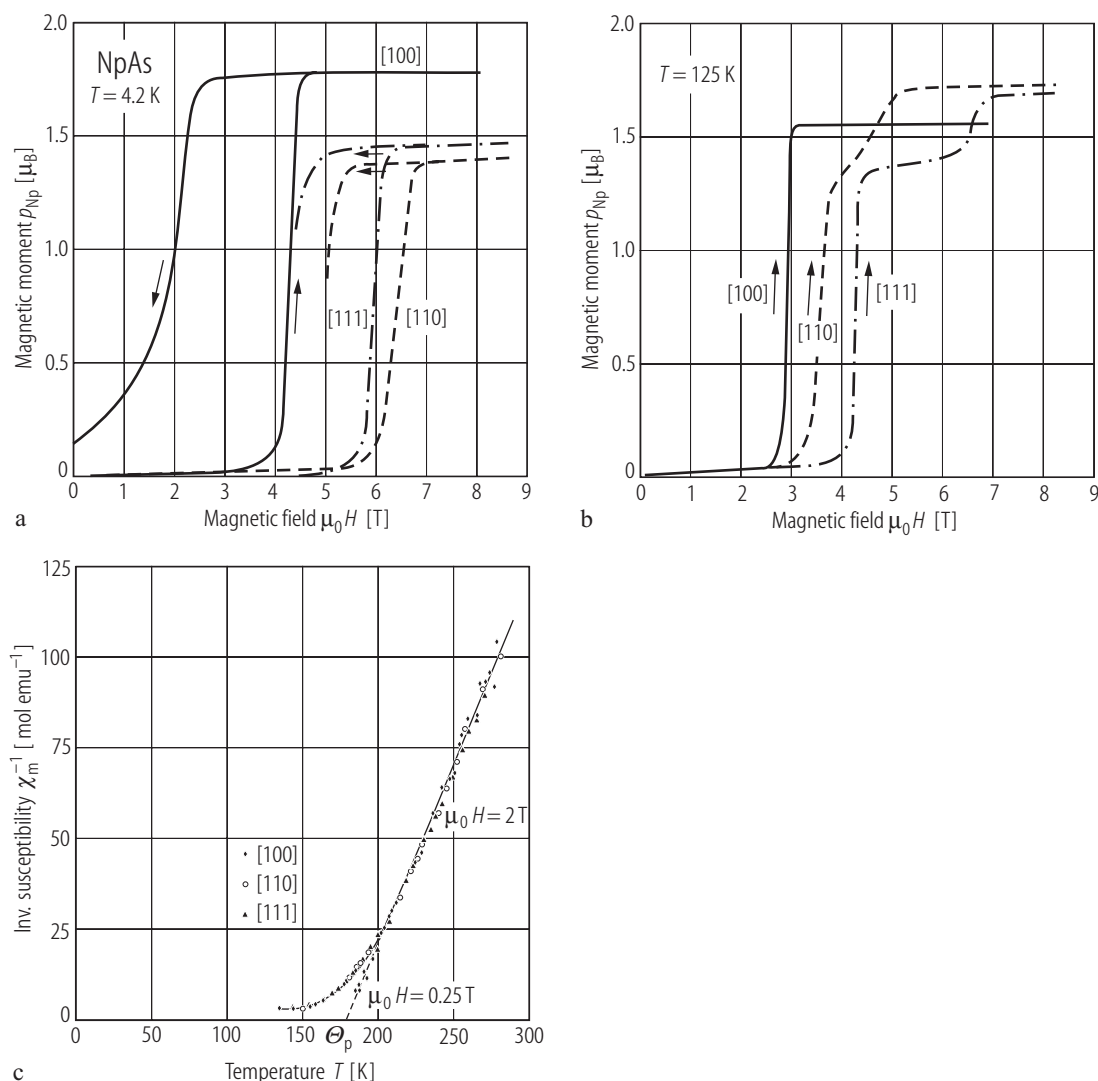


**Fig. IV.98.** NpAs s.c. (a) Magnetic moment  $p_{\text{Np}}$ , vs. applied magnetic field,  $H$ , measured at 4.2 K along the three main axes [92MVRS]. Note the metamagnetic transitions at higher fields. It is also assumed that at maximum applied field of about 8 T the full ferromagnetic state has not been reached and that at higher fields the system prefers to align along the [111] or [110] directions rather than along [100].

(b)  $p_{\text{Np}}$  vs.  $H$  at 125 K measured along three main directions [92MVRS]. Note two critical fields for the [110] and [111] curves, which implies also the change of the easy axis of magnetization. (c) Inverse molar susceptibility,  $\chi_m^{-1}$ , vs.  $T$  measured along three main crystallographic directions [92MVRS].  $\Theta_p = 176$  K,  $p_{\text{eff}} = 2.82 \mu_B$  in accordance with polycrystalline data of [74ADHL] (see also Fig. IV.97).

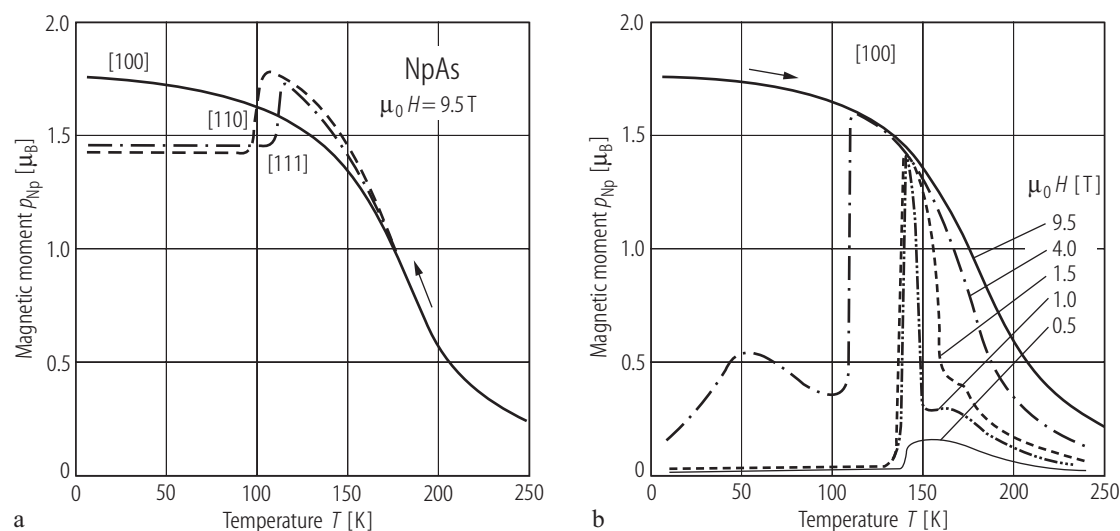


**Fig. IV.99.** NpAs s.c. **(a)** Magnetic moment,  $p_{\text{Np}}$ , vs. temperature,  $T$ , measured along three main crystallographic directions up to 250 K [92MVRS]. The change of the axis with maximum magnetization measured at 9.5 T takes place around 110 K, which coincides with the transition from a tetragonal to a cubic structure at  $T_0$  being stable at lower temperatures as derived on the basis of magnetization

and neutron diffraction studies. **(b)** Magnetic moment  $p_{\text{Np}}$ , along [100] vs. temperature,  $T$ , at various external magnetic fields from 0.5 to 9.5 T [92MVRS]. For comparison see the  $(H, T)$ -magnetic phase diagrams in Fig. IV.100 and Fig. IV.101a obtained from magnetization and neutron diffraction experiments, respectively.

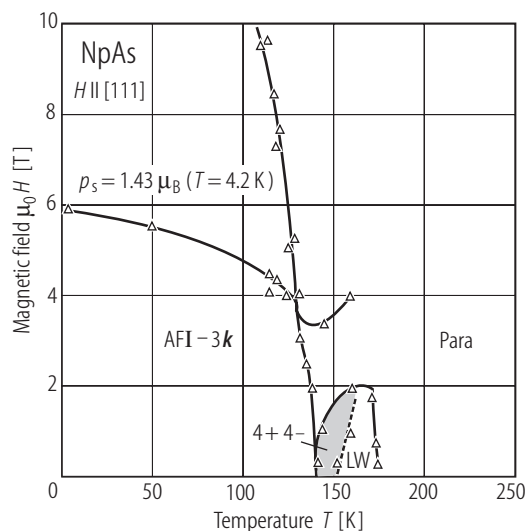


**Fig. IV.100.** NpAs s.c.  $(H, T)$  MPD inferred from the magnetization measurements for  $H$  along the [111] direction [92MVRS]. Note that the magnetic field shifts the tetragonal-to-cubic transition at  $T_0$  [i.e.  $(4+4-) \rightarrow (\text{AF } 1-3k)$ ], toward lower temperatures. Compare this diagram with that derived on the basis of neutron diffraction measurements [86BQKB] (see in Fig. IV.101a).

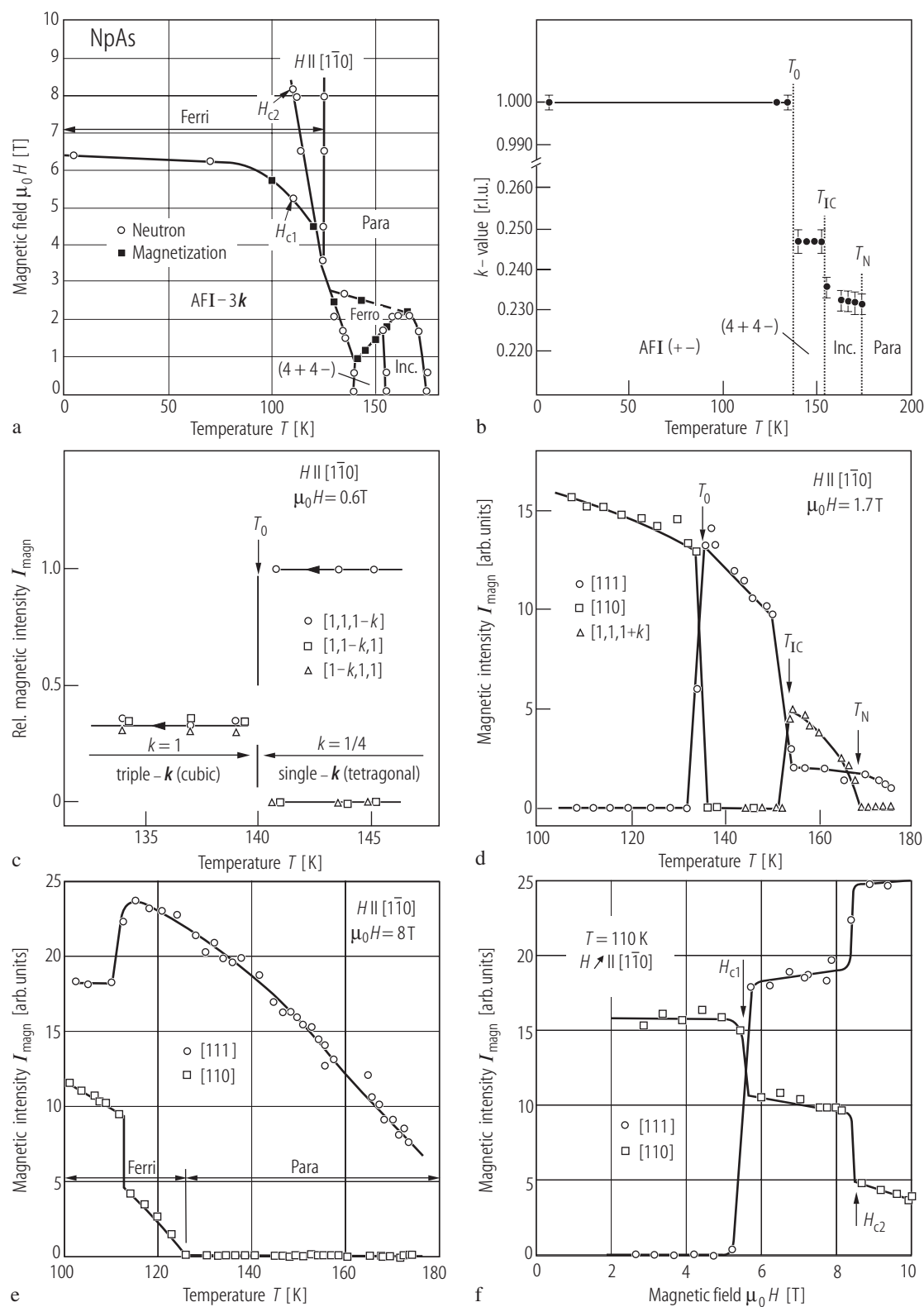


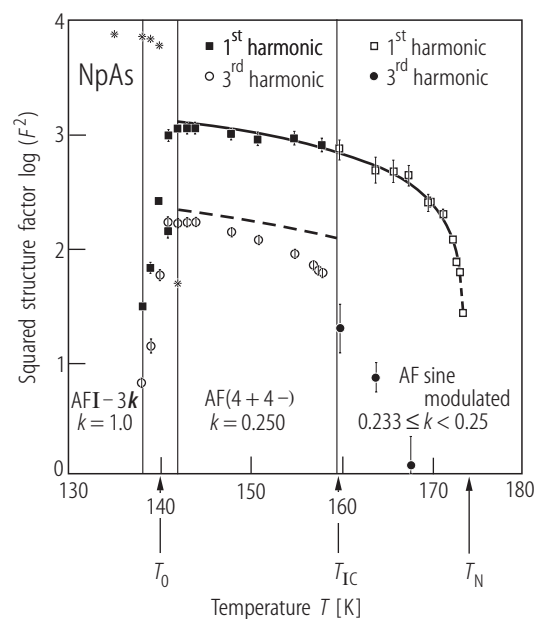
Fig. IV.101. For caption see next page.

**Fig. IV.101.** NpAs s.c. ND: **(a)**  $(H, T)$  MPD for  $H \parallel [1, \bar{1}, 0]$  [86BQKB], [87BBQR]. **(b)**  $k$ -value of the wave vector  $\mathbf{k} = [00k]$  vs. temperature,  $T$ , in zero applied magnetic field [86BQKB]. In  $H = 0$  NpAs orders antiferromagnetically at  $T_N = 173$  K with an incommensurate magnetic structure with  $k = 0.232 \pm 0.03$ . At  $T_{IC} = 154$  K a first-order lock-in transition occurs to the commensurate  $(4+, 4-)$  phase with  $k \approx 1/4$ . At  $T_0 = 138$  K another first-order transition yields the type I  $(+, -)$  phase with  $k = 1$  which persists down to the low temperatures. **(c)** Relative intensity of the magnetic peaks  $[1, 1, 1-k]$ ,  $[1, 1-k, 1]$  and  $[1-k, 1, 1]$ , vs. temperature,  $T$ , in the vicinity of the transition from the  $(4+, 4-)$  phase to the type I phase in a magnetic field of 0.6 T applied along the  $[1\bar{1}0]$  direction [86BQKB]. Clearly seen is the single- $\mathbf{k}$  to triple- $\mathbf{k}$  character of the transition, which explains the recovery of a cubic symmetry at the phase transformation (see Fig. IV.95). **(d)** Intensity of the magnetic peaks  $[111]$ ,  $[110]$  and  $[1, 1, 1+k]$ ,  $I_{\text{mag}}$ , vs. temperature,  $T$ , in a magnetic field of 1.7 T applied along the  $[1\bar{1}0]$  direction [87BBQR]. Below  $T_N = 169$  K an incommensurate collinear structure is observed down to  $T_{IC} = 152$  K where all superlattice magnetic reflections disappear. In between  $T_{IC}$  and  $T_0 = 133$  K only a ferromagnetic component is observed, which is aligned along a cubic axis and progressively turns toward the field direction with increasing the field strength. Below  $T_0$  the ordering corresponds to the triple- $\mathbf{k}$  type I structure. **(e)** Intensity of magnetic peak  $[111]$  and  $[110]$  vs. temperature,  $T$ , taken at 8 T applied along  $H \parallel [1\bar{1}0]$  [87BBQR]. Below  $T_N$  the one antiferromagnetic component with  $k = [001]$  (perpendicular to  $H$ ) coexists with a ferromagnetic component aligned along the applied field. **(f)** Intensity of the magnetic peaks  $[111]$  and  $[110]$ ,  $I_{\text{mag}}$ , vs. magnetic field,  $H$ , applied along  $[1\bar{1}0]$  at  $T = 110$  K [87BBQR]. The triple- $\mathbf{k}$  type I antiferromagnetic structure is stable up to  $\mu_0 H_{C1} = 5.4$  T where a first-order transition occurs into a ferromagnetic phase characterized by a single antiferromagnetic component,  $m_k$ , perpendicular to  $H$  and a ferromagnetic one, along a cube axis, i.e. at  $45^\circ$  from  $H$ . Another transition occurs at  $\mu_0 H_{C2} = 8.2$  T where the antiferromagnetic component is reduced and the ferromagnetic one rotates again from  $[100]$  to  $[1\bar{1}0]$ .

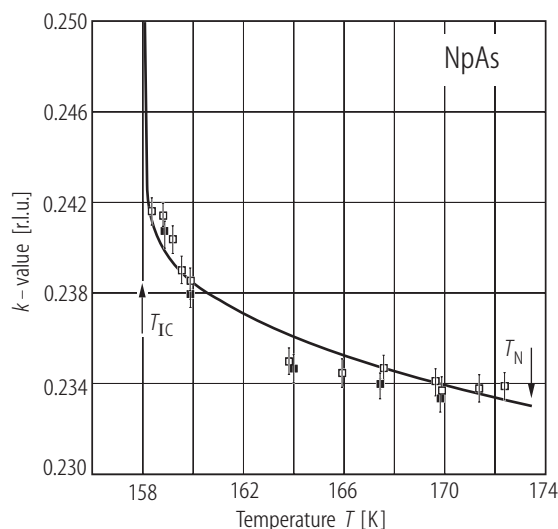
For the magnetic characteristics see the Table below.

**Table:** Characteristic of the main magnetic phases observed in the phase diagram of NpAs for  $H \parallel [1\bar{1}0]$ .

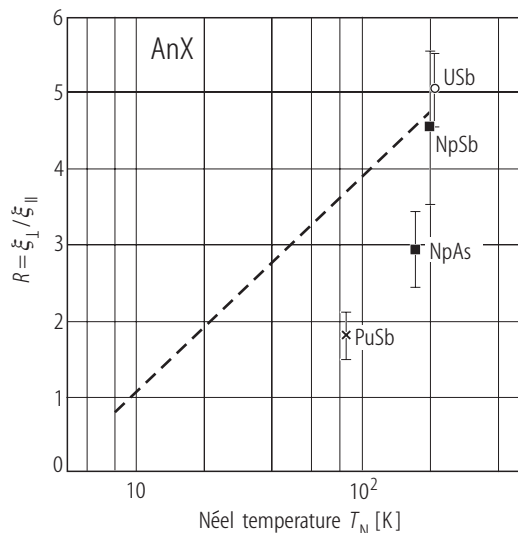
$T$	$\mu_0 H$	Ordering	AF-component			$p$ (ferro)		$p$ (total)
[K]	[T]		[ $\mu_B$ ]			[ $\mu_B$ ]		[ $\mu_B$ ]
			$m_{k1}$	$m_{k2}$	$m_{k3}$	Neutron	Magnetiz.	
4.2	0	Triple- $\mathbf{k}$ type I	1.64 $\pm 0.1$	1.41	1.63	0	0	2.6(1) [111]
	7	Ferri	0	0	1.12	2.3 $\parallel$ [100]	1.4	2.6(1) [201]
136	1.7	Ferro	0	0	0	2.0 $\parallel$ [100]	1.25	2.0(1) [100]
	6	Para	0	0	0	2.2 $\parallel$ [1 $\bar{1}$ 0]	1.55	2.2(1) [1 $\bar{1}$ 0]



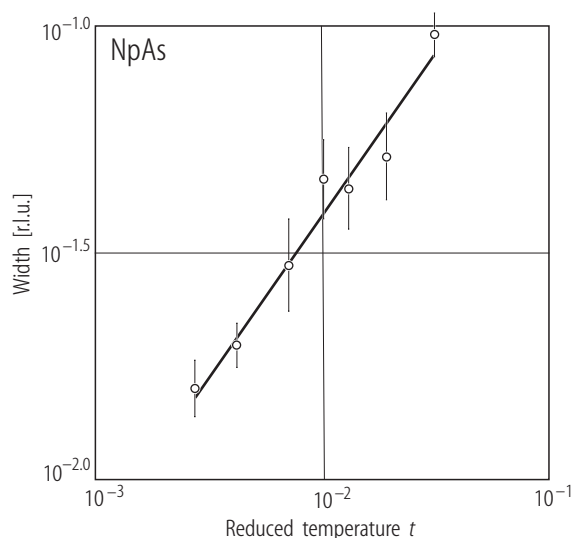
**Fig. IV.102.** NpAs s.c. ND: Details of  $(I_{\text{mag}}, T)$  MPD for  $T > 130$  K studied by neutron diffraction [91JSLR], [94LSLR2].  $T_N = 173.6$  K,  $T_{IC} = 158.2$  K and  $T_0 = 140$  K. The square of the structure factor as  $\log(F^2)$ , being proportional to the intensity,  $I_{\text{mag}}$ , as a function of temperature between 130 and 175 K. The solid curve through the first-order harmonics is the least squares fit to the  $\beta$ -parameter ( $= 0.38(1)$ ). The dashed line is the predicted intensity of the third-order harmonics in the case of a square wave modulation. As seen, the ideal square modulation, where  $A_3/A_1 = 0.1716$  ( $A_i$  are the wave amplitudes), is approached close to  $T_0$ . The stars mark the intensity of the  $(110)$  peak in type I-phase for  $T < T_0$ .  $p_{\text{Np}}$  (at 10 K) = 2.5(1)  $\mu_B$ . The change in the  $k$ -vector is accompanied by the growth in the third order harmonic, to obtain finally the commensurate value  $k = 1/4$ , having the square wave of the form  $++++- - - -$  or  $(4+ 4-)$  with  $(F_3/F_1)^2 = 0.17$ , and below  $T_0$ ,  $k = 1.0$ . This MPD is more detailed than that of [87BBQR], (see Fig. IV.101a).



**Fig. IV.103.** NpAs s.c. Modulation wave vector ( $k$ -value), vs. temperature,  $T$ , in the incommensurate region  $T_{IC} < T < T_N$  [91JSLR]. Open and closed symbols correspond to  $k$  determined from the first- and third-order harmonics. The solid line is a least-squares fit to the McMillan expression inferred originally for structural modulations (for details see the text of original paper). Note that despite a rapid growth of  $k$  at temperatures close to  $T_{IC}$ , the transition at this temperature is continuous, as it has been predicted. The fitted values of the McMillan equation are:  $T_{IC} = 158.2(5)$  K,  $k_C = 0.25$ ,  $k_{IC} = 0.233$  rlu (see [92JLSL]).

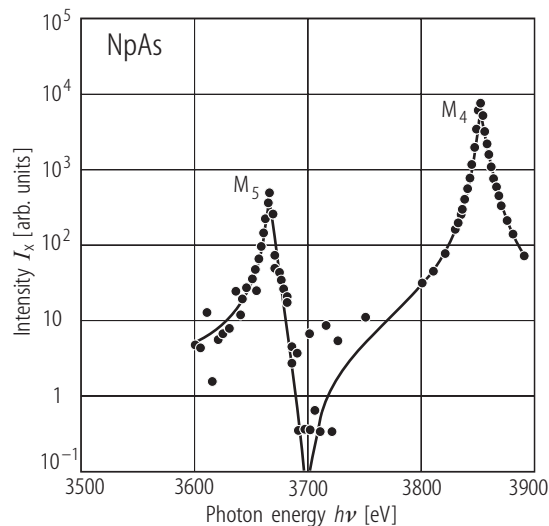


**Fig. IV.106.** NpAs, USb, NpSb, PuSb. Correlation range ratio,  $R = \xi_{\perp} / \xi_{\parallel}$ , vs.  $\log T_N$  for the neptunium and plutonium mononictides [91LA], [93L2], compared (dashed line) to those of cerium and uranium mononictides given by [84HF] and presented in Fig. R.36b as a straight line. Note that the highest values of  $R$  are obtained for those mononictides having the highest  $T_N$  and the triple- $k$  structure. For discussion in terms of direct 5f-np electron mixing see [81SLSV] and [87BRLS].

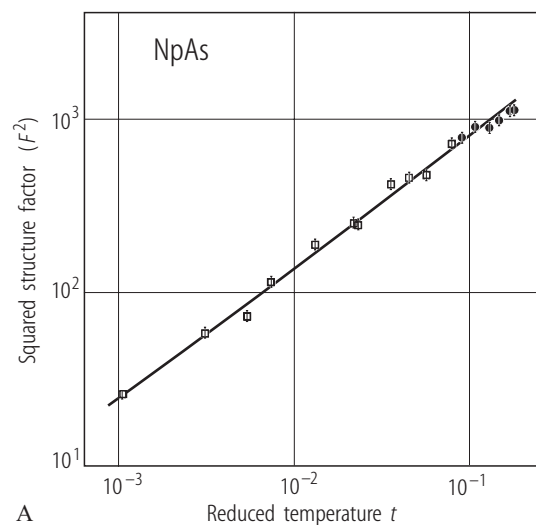


**Fig. IV.105.** NpAs s.c. Inverse correlation lengths  $\kappa_{\parallel}$  (parallel to the direction of wave vector in the  $[00\eta]$  direction) vs. reduced temperature,  $t$ , on a double logarithmic scale [91JSLR]. The solid line is the least squares fit of  $\kappa = \kappa_0 t^{\nu}$  to experimental points which gives  $\nu = 0.73(2)$ . The anisotropy parameter  $R = \kappa_{\parallel} / \kappa_{\perp} = 2.9(5)$ .

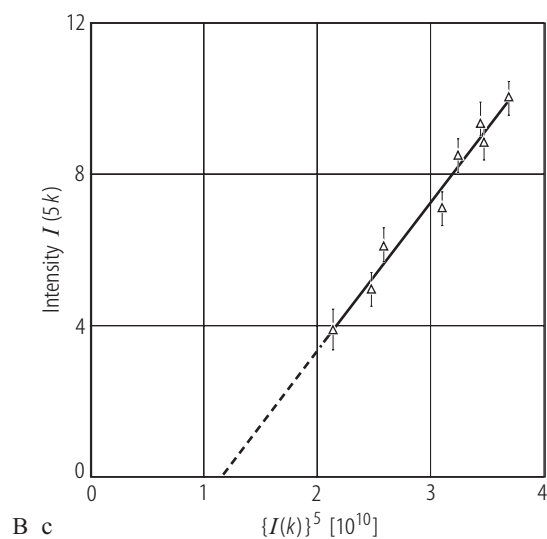
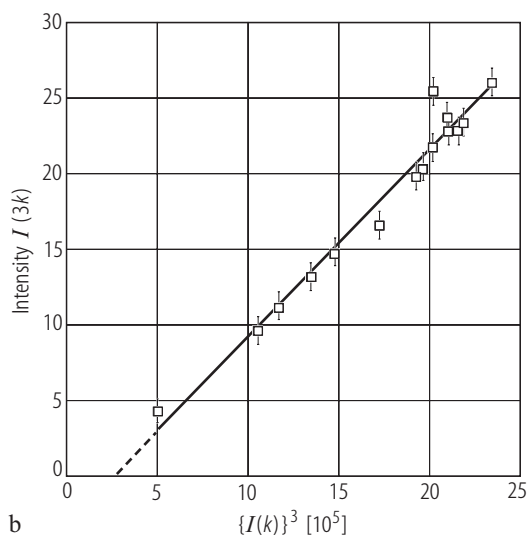
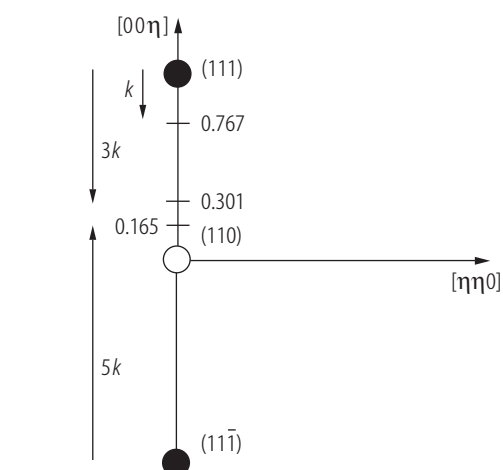
For Fig. IV.104 see next page



**Fig. IV.107.** NpAs s.c. RXMS: Intensity of scattered X-rays,  $I_x$ , vs. photon energy  $h\nu$  [92LS], [94LSLR2]. The solid line is a fit to the two-resonance dipole model as inferred from atomic physics. They are located at the absorption edges and have the Lorentzian form. The resonances corresponding to those at the  $M_5$ - and  $M_4$ -edges are at 3666(5) eV and 3852(5) eV, respectively.



**Fig. IV.104.** NpAs s.c. **(A)** Integrated intensity (square of structure factor,  $F^2$ ), vs. reduced temperature,  $t$ , for the 1<sup>st</sup> order harmonics measured below  $T_N$  ( $= 173.64(5)$  K) on a double logarithmic scale [91JSLR]. The least squares fit (solid line) of  $F^2 = F_0^2 t^{2\beta}$  to experimental data gives  $\beta = 0.38(1)$  which holds for incommensurate ( $T < T_N$ ) and commensurate ( $T < T_{IC}$ ) phases (3D Heisenberg  $\beta \approx 0.345$ ). Open and closed symbols correspond to Bragg peaks taken above and below the transition temperature  $T_{IC}$  ( $= 158.2$  K). **(B)** **(a)** Neutron critical scattering planes (Brillouin zone center  $\Gamma$  (open circles) and a zone boundary X (closed circles). The integrated intensities of **(b)**  $3k$ - and **(c)**  $5k$ -order harmonics following the Landau theory (solid lines) show that the magnetization ( $M_{nq}$ ) of harmonics is proportional to  $|M_q|^n$  [92JLSL].





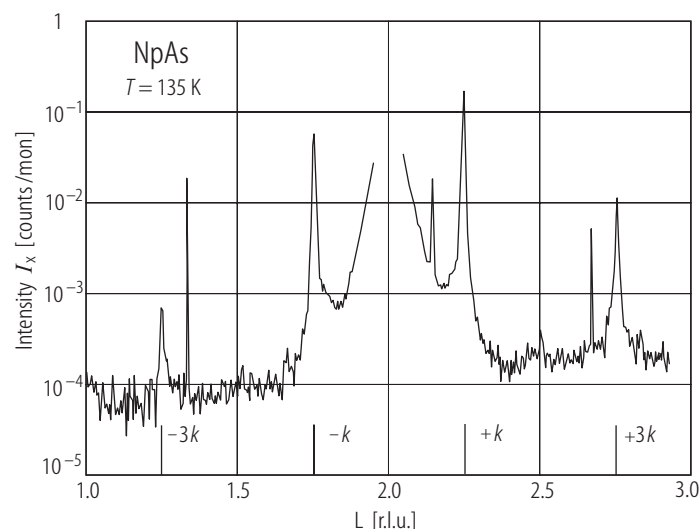


**Fig. IV.108.** NpAs s.c. RXMS: Experimental X-ray scan ( $\log I_x$ ) made at the Np  $M_4$  resonant energy (see Fig. IV.107) of  $E = 3.852$  keV along the L direction from the (001) face at  $T = 135$  K. At  $L = 2$  the main charge scattering peaks. Peaks at  $\pm 1k$  and  $\pm 3k$  are magnetic. The remaining peaks are from beam and holder contamination. See refs. [94LSLT] and [95LSLG].

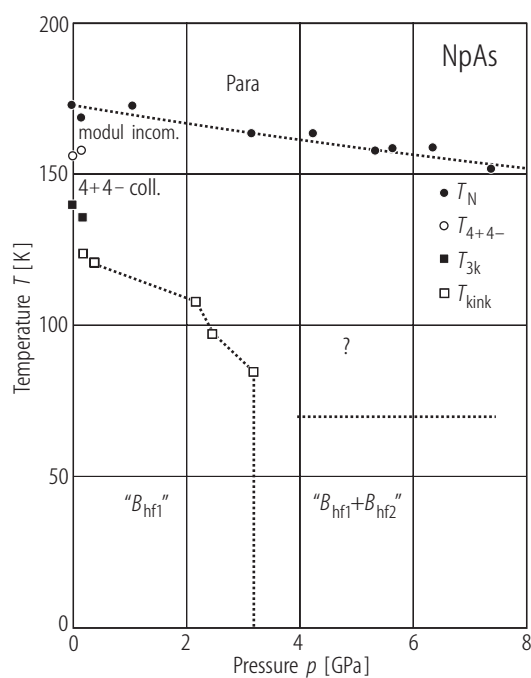


**Fig. IV.109.** NpAs. RXMS: Tentative magnetic phase diagram ( $T, p$ ) [97IZBS].  $T_N$  (closed circles),  $T_{4+4-}$  (open circles),  $T_{3k}$  (closed squares) and  $T_{kink}$  (open squares) are the Néel temperature, transition temperature to the AF phase (4+4-), transition temperature into AF I-3 $k$  phase and transition temperature into new high-field phases, respectively. The phases marked by " $B_{hf1}$ ", " $B_{hf1}+B_{hf2}$ ", and that marked by "?" denote unknown high-pressure phases to be determined. (Here:  $T_0 \equiv T_{3k}$  and  $T_{IC} \equiv T_{4+4-}$ ).

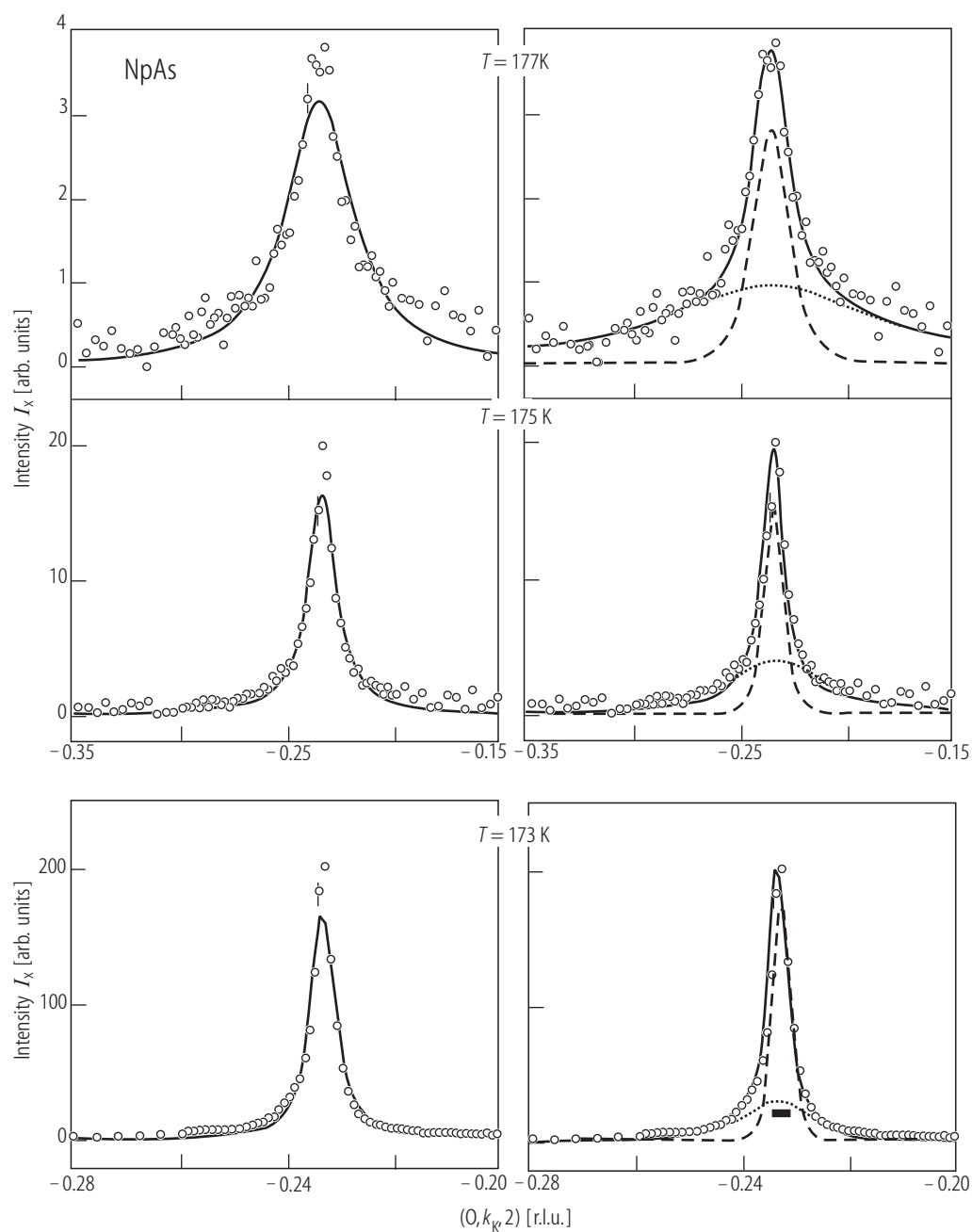


**Fig. IV.110.** NpAs s.c. RXMS: Critical scattering intensity vs. the reciprocal space position  $(0, k_y, 2)$  for three temperatures taken above  $T_N (= 172.8(2)\text{ K})$  [94LSLR3]. The left and right hand panels show a single-component Lorentzian fit to the data and the fit to the 2-component model, respectively. The full line in the latter case is the

sum of the Lorentzian  $L$  (dotted line) and Lorentzian-squared  $L^2$  (dashed line) components (for the corresponding equations see the text of the original paper). The instrument resolution is marked by the horizontal bar (bottom). Note different scales at various temperatures

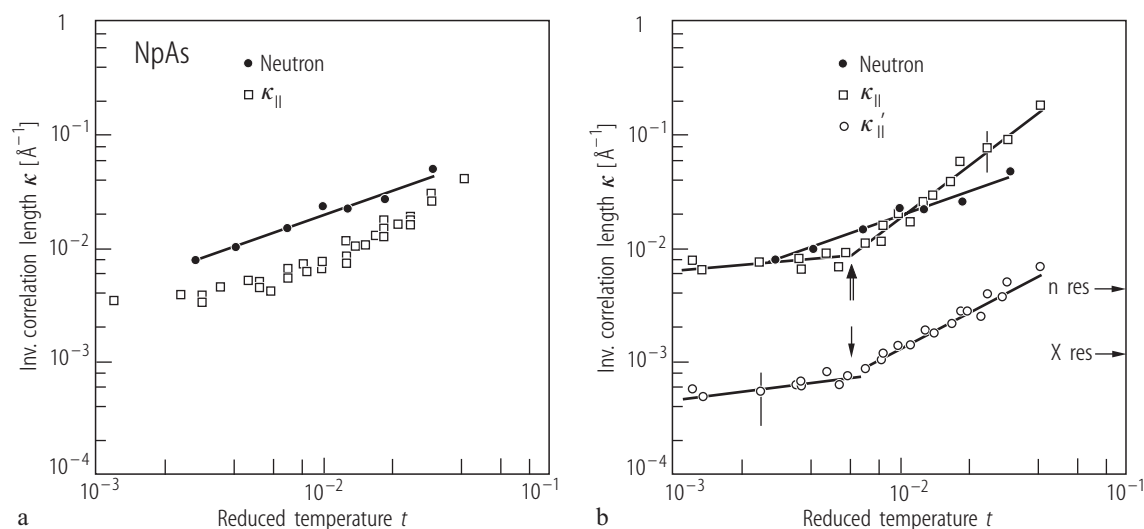


**Fig. IV.111.** NpAs s.c. RXMS: The deconvoluted inverse correlation length,  $\kappa$ , vs reduced temperature,  $t$ : **(a)** for the single-Lorentzian model ( $\kappa_{||}$ ), and **(b)** for both Lorentzian ( $\kappa_{||}$ ) (open squares) and Lorentzian-squared ( $\kappa'_{||}$ ) (open circles) two-component model [94LSLR1,3]. These X-ray scattering results are compared to the neutron results of Ref. [91JSLR] (closed circles), which show no evidence of the two-component case. Note a double logarithmic scale. The

horizontal arrows mark the instrumental resolution. The correlation length exponent  $\nu$ , where  $\kappa_i = \kappa_0 t^{\nu_i}$ , found in neutron and X-ray experiments, appears to be different.  $\nu(\text{neutron}) = 0.73(2)$ ,  $\nu(\text{X-ray broad}) = 1.5(3)$ ,  $\nu(\text{X-ray sharp}) = 1.0(2)$ , while  $\nu(3D \text{ Heisenberg}) = 0.707$ . The changes in the slope at  $t \approx 6 \cdot 10^{-3}$  (arrows) arise from the combination effects, i.e. the presence of two components complicates the determination of  $\nu$ .

**Fig. IV.112.** NpAs s.c. RXMS: Three types of magnetic domains A, B and C along the H, K, and L lines in reciprocal space are possible. For explanation see [94LSLR2]. **(a)** The figure presents the temperature change in the C-type domains. On cooling through  $T_N$ , the C domain population is reduced being not favoured by dipole interactions, while at lower temperatures a dramatic change takes place and the material becomes a single-C domain. This domain has their moments perpendicular to the surface of the crystal, while for the A and B domains the moments lie in the surface plane. The rapid increase in the population of C domains may be considered as a new kind of phase transition ( $T_i \approx 135 \text{ K}$ ) in which the spontaneous domain reorientation becomes a precursor of the first-order phase transition to the  $3k$ -magnetic structure at  $T_0$ . The horizontal arrow indicates the value of  $1/3$ , expected for a random distribution of domains, followed in the case of neutron experiment. The behaviour in the C domains population introduces the serious difference between the two kinds of experiments. **(b)** The magnetic wave vector values  $k_L(k_K)$  as a function of temperature,  $T$ , shown as closed (open) symbols. They correspond to different C(b) domains with the moments perpendicular (parallel) to the surface [94LSLR2] and [94LSLT]. **(c)** The magnetic scattering intensity,  $I_s$ , in the  $[0, k_K, 2]$  direction of scans taken at different temperatures around  $T_N$  [94LSLR3] and [94LSLT]. Note the logarithmic intensity scale. The small black bar indicates the instrumental resolution.  $T_N = 172.8 \text{ K}$ . **(d)** Experimental scans,  $I_s$ , vs.  $k_L$  along the L-axis (C-type domains) at temperatures ( $145 < T < 153 \text{ K}$ ), around  $T_{IC}$  [94LSLR2]. The wave vector,  $k_L$ , changes from  $k_{IC} = 0.233 \text{ r.l.u.}$  at  $153 \text{ K}$  to  $k_C = 0.250 \text{ rlu}$  at  $148 \text{ K}$ , but at intermediate temperatures two peaks  $k_{IC}$  and  $k_C$  coexist which, in addition, exhibit considerable broadening. **(e)** Experimental scans  $I_s$  vs.  $k_K$  along the K-axis for the B-type domains at  $152.5 \text{ K}$  [94LSLR2]. Note two sharp peaks at the extreme values ( $k_{IC} = 0.233$  and  $k_C = 0.25$ ) and in addition a broad peak at an intermediate value  $k_K$ . Both above cases (figures (d) and (e)) indicate a high wave vector resolution of X-ray magnetic scattering.

For Fig. IV.112 see next page

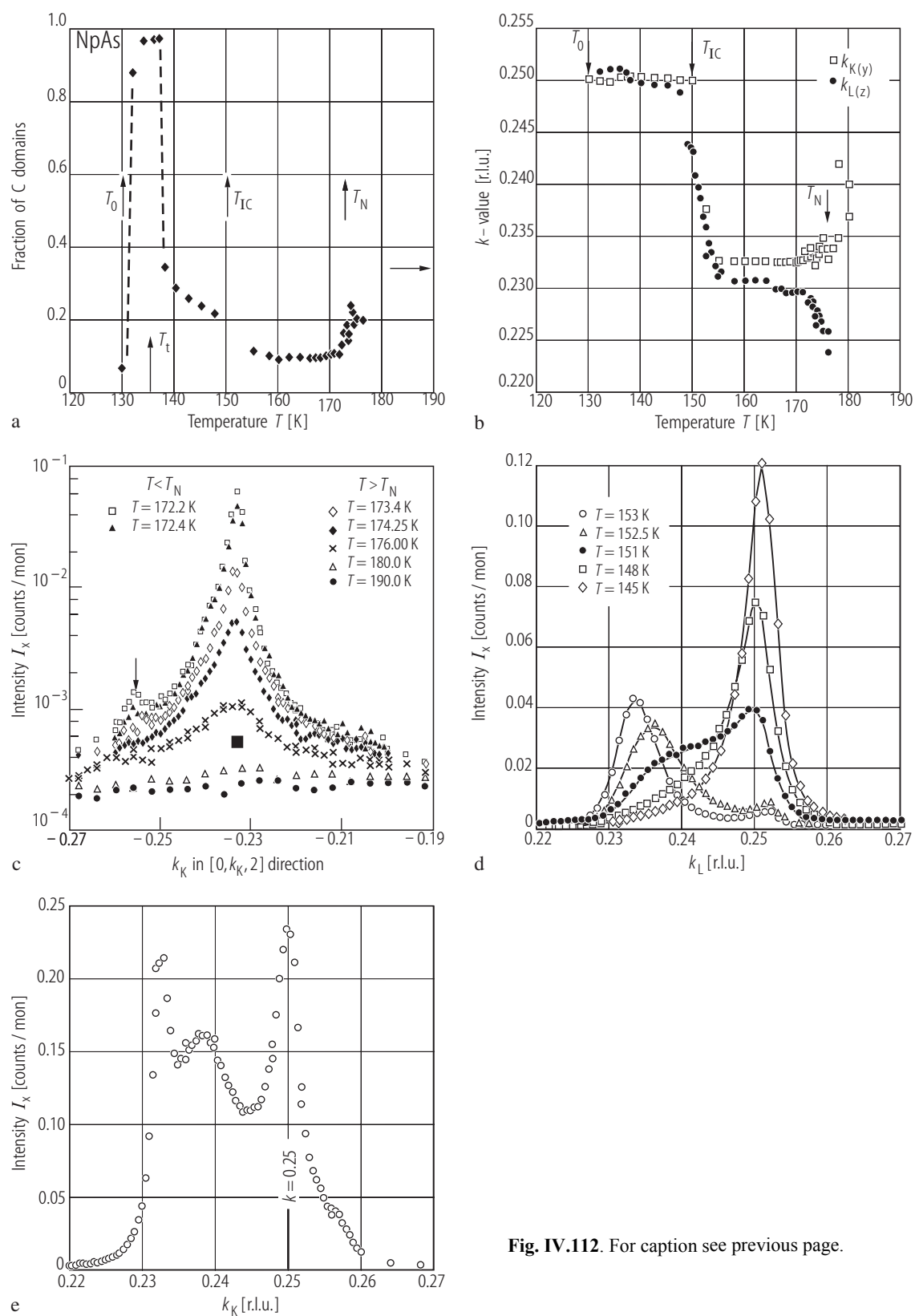
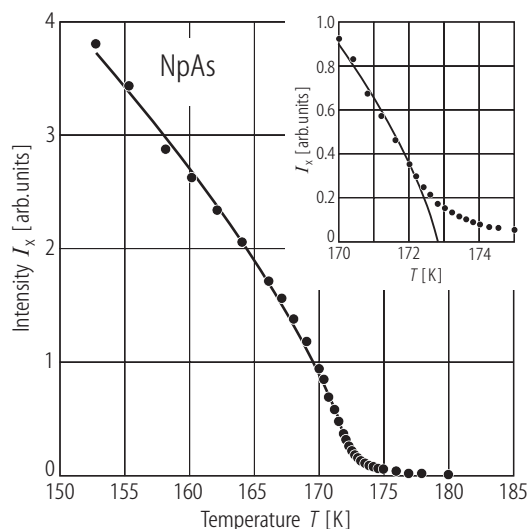
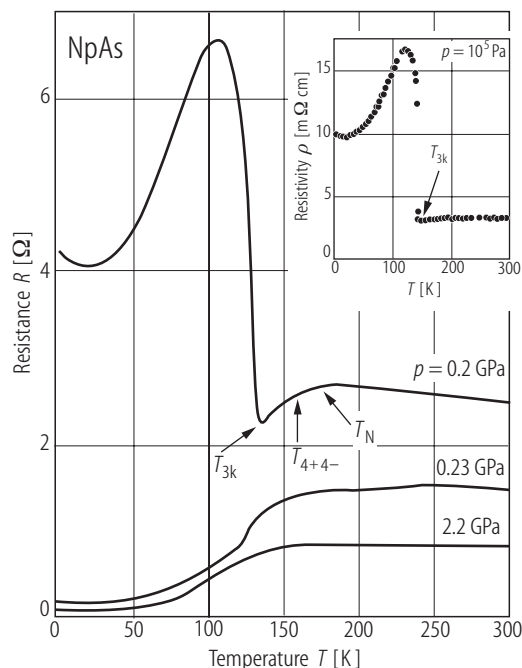
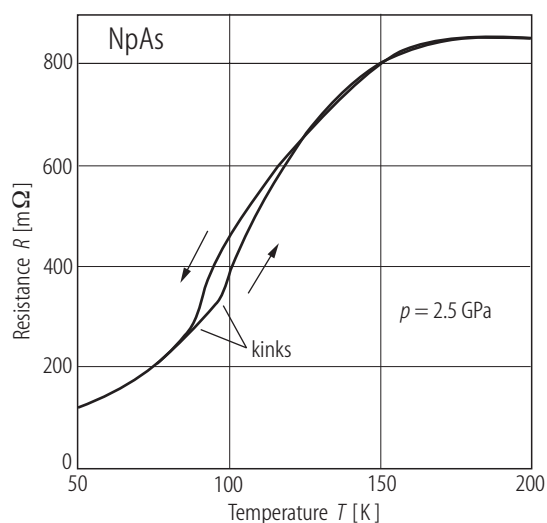


Fig. IV.112. For caption see previous page.



**Fig. IV.113.** NpAs s.c. RXMS: The integrated intensity,  $I_x$ , of the magnetic satellite at wave vector  $(0,k,2)$  vs. temperature,  $T$ , around  $T_N$  [94LSLR1]. The solid line is a fit to the power law  $I = I_0 t^{2\beta}$ , ( $t$ : reduced temperature), where  $\beta = 0.36(2)$  and  $T_N = 172.8(2)$  K. These results can be compared to the neutron experiment which gave  $T_N = 173.6(1)$  K and  $\beta = 0.38(1)$  [91JSLR]. The Heisenberg model gives  $\beta = 0.367$ . The inset presents the behaviour at temperatures very close to  $T_N$ .



**Fig. IV.114.** NpAs s.c. Electrical resistance,  $R$ , vs. temperature,  $T$ , measured under pressure between 0.2 and 2.2 GPa [97IZBS]. The arrows show three transition temperatures:  $T_N$ ,  $T_{4+4-}$  (or  $T_{IC}$ ) and  $T_{3k}$ , (or  $T_o$ ), which determine the Néel temperature transition from the incommensurate to commensurate 4+4- structure and the onset of the AF I-triple  $k$  structure, respectively. The inset presents the ambient data taken from [90P] and [93FG]. Note both a strong increase of  $\rho$  appears at the onset of the  $3k$  magnetic structure ( $T_{3k} \approx 140$  K) associated with the formation of a new BZ (see [95K2]) and that considerable quantitative changes take place under applying pressures. In the paramagnetic range a logarithmic variation of the resistance points to a Kondo behaviour. See similar  $R(T)$  behaviour measured on the polycrystalline sample of NpAs by [74ADHL].

**Fig. IV.115.** NpAs s.c. Electrical resistance,  $R$ , vs. temperature,  $T$ , measured under pressure of 2.5 GPa [97IZBS]. Note a kink at  $\sim 120$  K, which manifests a positive  $R(T)$  curvature for  $T < 120$  K and a negative one for temperatures  $T > 120$  K. At several pressures the kink exhibits a strong hysteresis upon decreasing and increasing temperature. As pressure is increased  $T_{\text{kink}}$  decreases and disappears above 3 GPa.

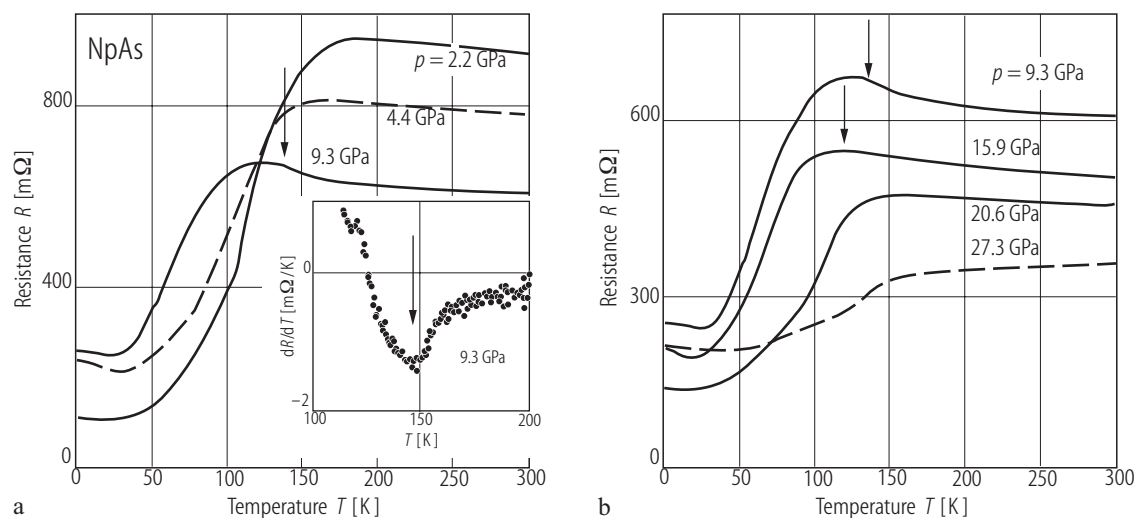


**Fig. IV.116.** NpAs s.c. Electrical resistance,  $R$ , vs. temperature,  $T$ , measured under pressures (a) from 2.2 up to 9.3 GPa and (b) from 9.3 up to 27.3 GPa [97IZBS]. The arrows point to the temperatures of predicted magnetic

order, extracted from the derivative  $dR(T)/dT$  (for an example see the inset). Note that the  $R_{300\text{K}}/R_{4.2\text{K}}$  ratios decrease considerably with increasing pressure.

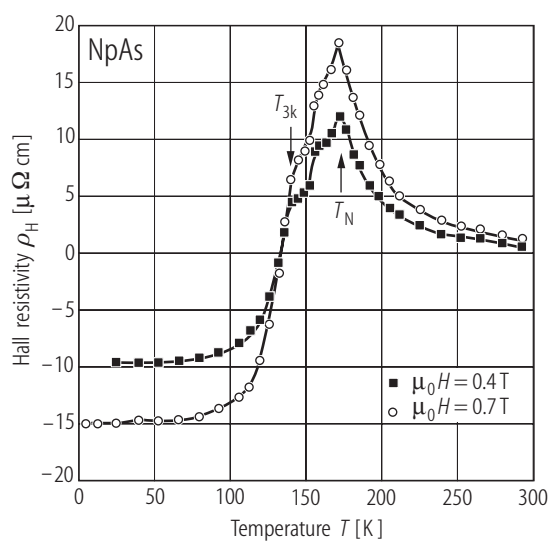


**Fig. IV.117.** NpAs. Hall resistivity,  $\rho_H$ , vs. temperature,  $T$ , measured at two applied magnetic fields  $\mu_0 H = 0.4$  and  $0.7$  T. [93FG]. The analysis of the data shows the change in the normal Hall coefficient  $R_0$  from about  $0.9 \cdot 10^{-8} \text{ m}^3/\text{C}$  in the paramagnetic state to about  $21.5 \cdot 10^{-8} \text{ m}^3/\text{C}$  in the triple- $k$  phase which is connected with a strong reduction of the number of conduction electrons. Simultaneously the anomalous Hall coefficient  $R_S$  decreases from about  $700 \cdot 10^{-8} \text{ m}^3/\text{C}$  in the paramagnetic range to the very low value of about  $3 \cdot 10^{-8} \text{ m}^3/\text{C}$  at 50 K.

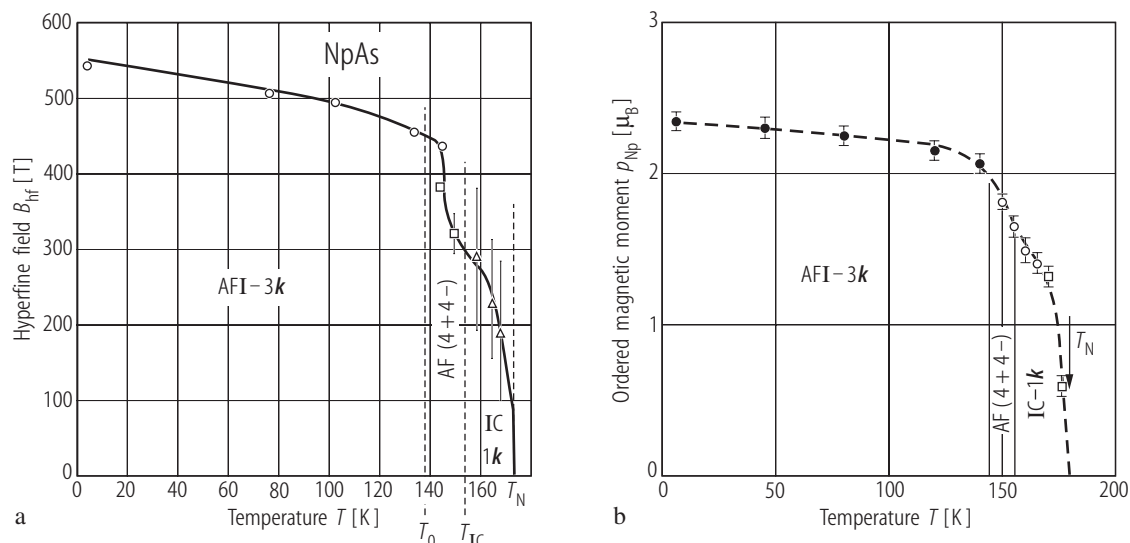


**Fig. IV.118.** NpAs. **(a)** Hyperfine field,  $B_{\text{hf}}$ , vs. temperature,  $T$ , [89K], [89PMPZ]. Note the sudden drop in  $B_{\text{hf}}$  by 10% at the transition from the non-collinear structure to the collinear 4+4- structure around  $T_0$  (= 138 K) with agreement of neutron diffraction results [86BQKB]. At

temperatures between  $T_{\text{IC}}$  (= 153 K) and  $T_{\text{N}}$  the Mössbauer spectra show broad lines resulting from distribution of hyperfine fields. **(b)** ND magnetic phase diagram in the form of the ordered magnetic moment  $p_{\text{Np}}$  as a function of temperature [74ADHL].

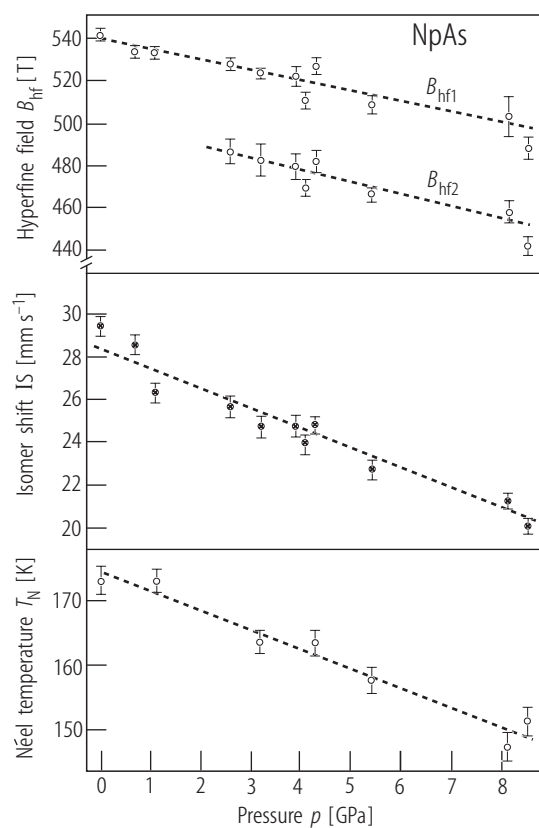


**Fig. IV.119.** NpAs. Hyperfine fields,  $B_{\text{hf1}}$  and  $B_{\text{hf2}}$ , isomer shift,  $\text{IS}$ , (relative to the Am source), and Néel temperature  $T_{\text{N}}$  as a function of pressure,  $p$ , [89PMPZ]. Note that at ~2.5 GPa a second hyperfine field  $B_{\text{hf2}}$  appears, confirming the earlier report [87PMPL]. The volume coefficients are as follows:  $d \ln p_{\text{Np}} / d \ln V = -0.8$  and  $\partial \ln T_{\text{N}} / \partial \ln V = -1.3$ . These values are about one order of magnitude less than those for UN, -19 and -19, respectively (see [94KZGN]).

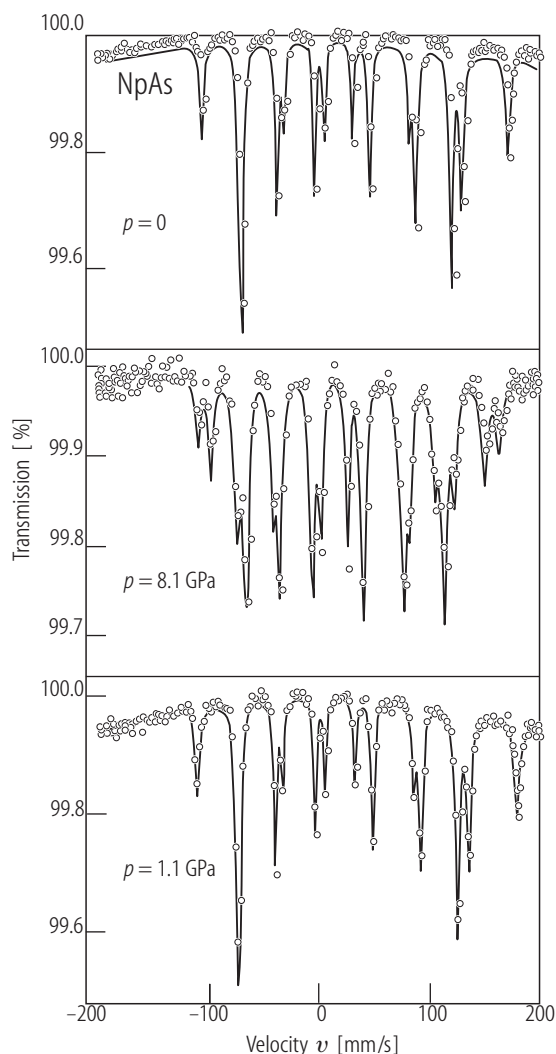


**Fig. IV.120.** NpAs.  $^{237}\text{Np}$  Mössbauer spectra taken at 4.2 K at ambient and at pressures of 1.1 and 8.1 GPa [87PMPL].

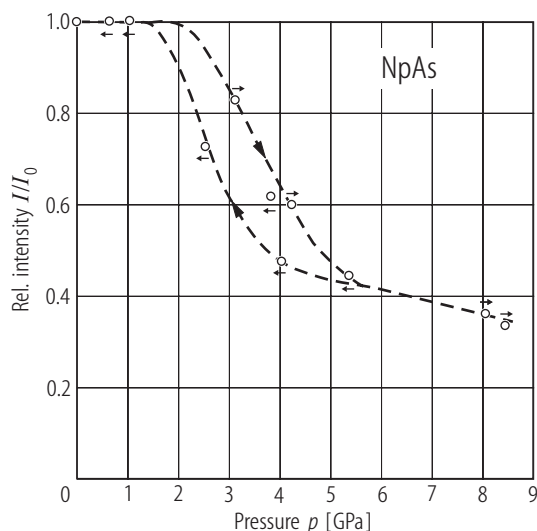


**Fig. IV.121.** NpAs. Relative intensity,  $I/I_0$ , of the Zeeman pattern with the larger value of  $B_{\text{hf}}$  with increasing and decreasing pressures up to 8.6 GPa [90K]. Such a behaviour arises from the coexistence of two magnetic structures (probably antiferromagnetic non-collinear with collinear 4+4- one) over a wide pressure range. Compare  $(T, p)$  magnetic phase diagram presented in Fig. IV.109.

For Fig. IV.122 see next page

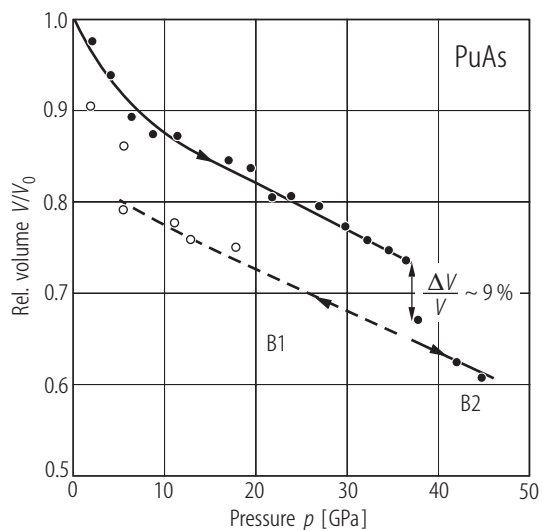


**Fig. IV.123.** PuAs. Relative volume,  $V/V_0$ , vs. pressure,  $p$ , up to 45 GPa [89BDDL].  $a_0 = 0.58565(5)$  nm. The B1→B2 transformation takes place at 37 GPa with increasing pressure (closed circles) and hysteresis lasts down to 5 GPa with decreasing pressure (open circles). See Tables 5 and 6.



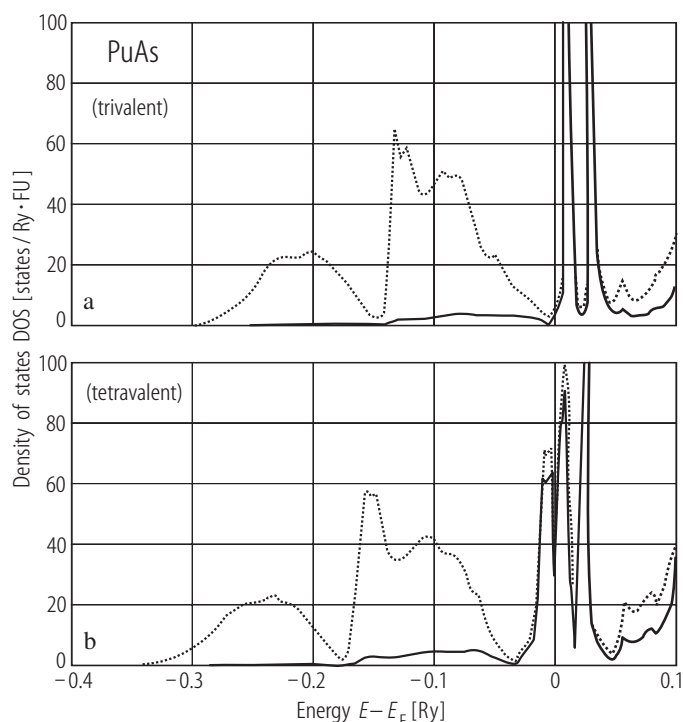


**Fig. IV.122.** PuAs. *Ab initio* energy band structure by the self-interaction-correlated (SIC)–LSD approximation; DOS (states/Ry FU) [02PSTS]. **(a)** The trivalent Pu configuration ( $\text{Pu}^{3+}, 5f^5$ ),  $p_{\text{eff}} = 0.84 \mu_{\text{B}}$ , **(b)** the tetravalent Pu configuration ( $\text{Pu}^{4+}, 5f^4$ ),  $p_{\text{eff}} = 2.68 \mu_{\text{B}}$ . The remaining f-states are allowed to delocalize, which leads to hybridization with the anion p-band and gives rise to narrow peaks (solid lines), just above  $E_{\text{F}}$ . Next, they are broadened due to considerable f-d hybridization. In case **(a)** the three valence electrons of Pu are transferred to the p-band being only half filled, the sharp f-p hybridized peaks appear just above  $E_{\text{F}}$ . Thus, the trivalent configuration was found to be more stable for all PuX, except for PuN. For the latter it is even pentavalent configuration ( $5f^3$ ) predicted as mostly stable. In case **(b)** there is one more f-d peak and one more band electron, which fills up the lowest lying f-d peak. This is rather regarded as unfavourable configuration for AnX, with X = P...Bi. The dotted and solid lines represent the total DOS and the f-projected DOS, respectively.

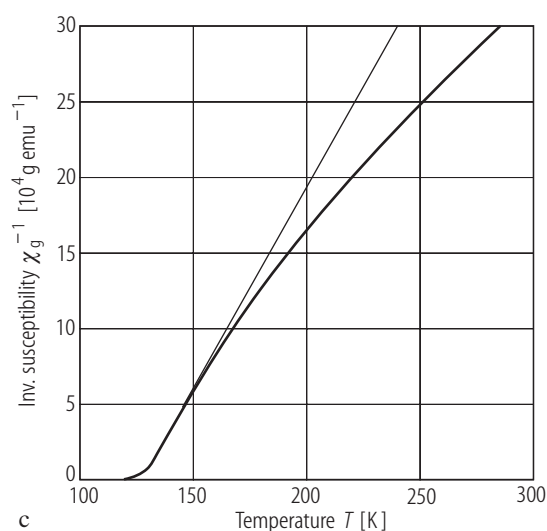
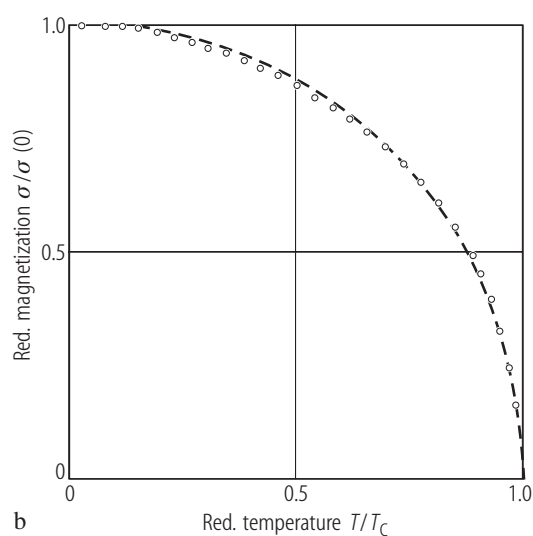
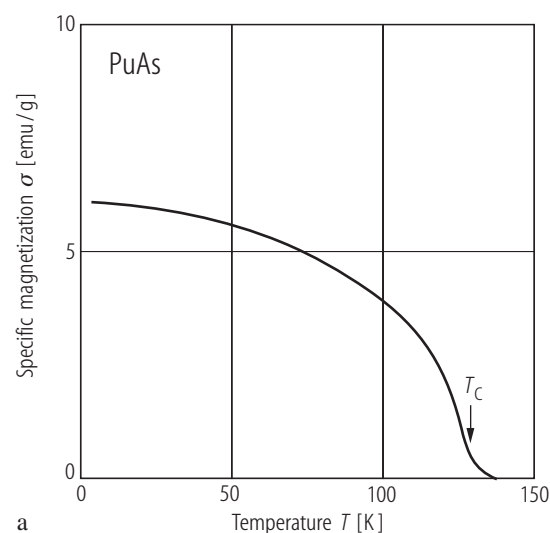


**Fig. IV.124.** PuAs. **(a)** Specific magnetization,  $\sigma$ , vs. temperature,  $T$ , measured on a polycrystalline sample [73BFS].  $T_C = 129$  K. **(b)** Reduced magnetization,  $\sigma(T)/\sigma(0)$ , vs. reduced temperature,  $T/T_C$  [73BFS].  $p_S = 0.3 \mu_B$ . The dashed curve is the Brillouin function  $B(J = 5/2)$ . **(c)** Inverse specific magnetic susceptibility,  $\chi_g^{-1}$ , vs. temperature,  $T$  [73BFS]. MCW-law:  $\chi_0 = 0.33(5) \cdot 10^{-3} \text{ emu/mol}$ ,  $\Theta_p = 128.8(1)$  K and  $p_{\text{eff}} = 0.97(5) \mu_B$ . For  $\text{Pu}^{3+}$  in Russell-Saunders scheme:  $p_{\text{eff}} = 0.85 \mu_B$  and  $p_S = 0.715 \mu_B$ .

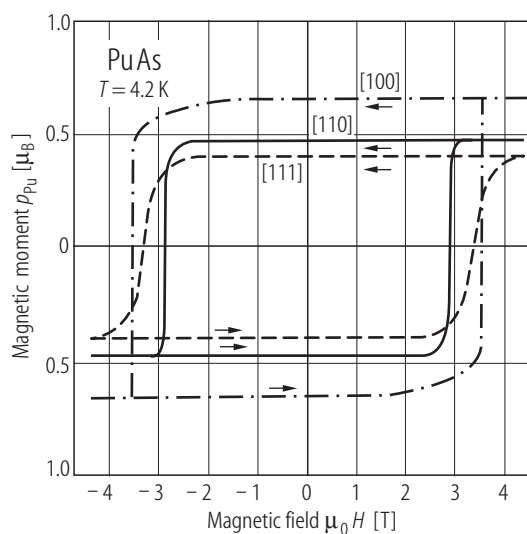


**Fig. IV.125.** PuAs s.c. Magnetic moment  $p_{\text{Pu}}$  vs. applied magnetic field,  $H$ , at 4.2 K along three main crystallographic directions [86MVSR2]. As is evidenced by the width of the hysteresis loops, the domain walls have to be very narrow here.  $p_S[100] = 0.67 \mu_B$  which is lower than  $p_0 = 0.75 \mu_B$  determined by neutron-diffraction measurements [84BQRS].

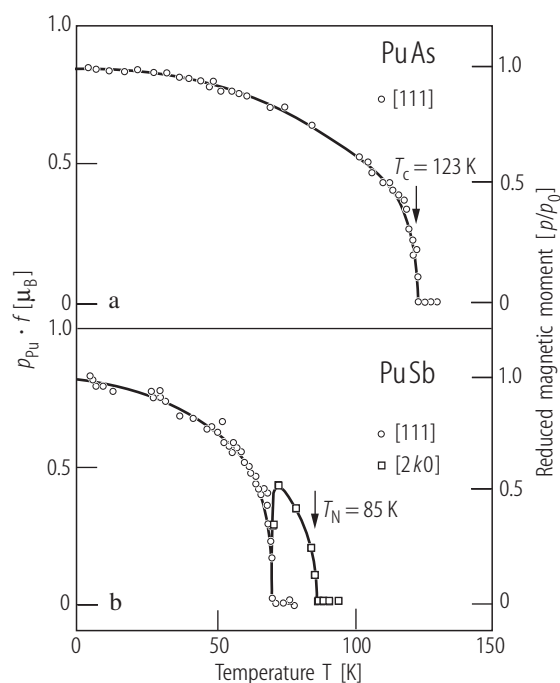


**Fig. IV.126.** PuAs, PuSb s.c. Neutron diffraction experiment. The product  $p_{\text{Pu}} \cdot f(Q)$  for the (111) reflection as a function of temperature,  $T$ , [84BQRS].  $f(Q)$  is the 5f form factor. **(a)** PuAs: it develops ferromagnetism below  $T_C = 123(1)$  K with  $p_0 = 0.75(10)$   $\mu_B$ . **(b)** PuSb: it first develops antiferromagnetism below  $T_N = 85$  K and then ferromagnetism below  $T_C = 67$  K [84BQRS].  $p_0 = 0.74$   $\mu_B$ .

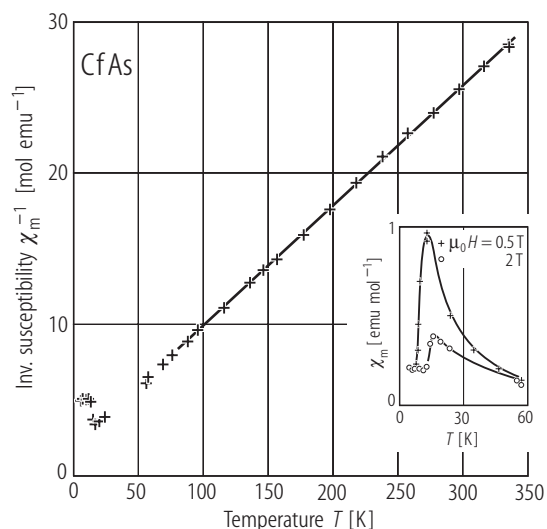


**Fig. IV.128.** CfAs. Inverse molar magnetic susceptibility,  $\chi_m^{-1}$ , vs. temperature,  $T$ , [87HN]. The solid line is a Curie-Weiss fit in the region 80...340 K yielding  $\Theta_p = -29$  K and  $p_{\text{eff}} = 10.1$   $\mu_B$ . The moment value is in accordance with the intermediate coupling values for the  $f^9$  ( $\text{Cf}^{3+}$ ) and  $f^{10}$  ( $\text{Cf}^{2+}$ ) configurations, which are 10.2 and 10.3  $\mu_B$ , respectively. The inset displays the low-temperature behaviour of  $\chi_m$  vs.  $T$  measured at two applied magnetic fields 0.5 (crosses) and 2 T (open circles). The maximum in  $\chi_m(T)$  at about 17.5 K is a signature of an antiferromagnetic ordering.

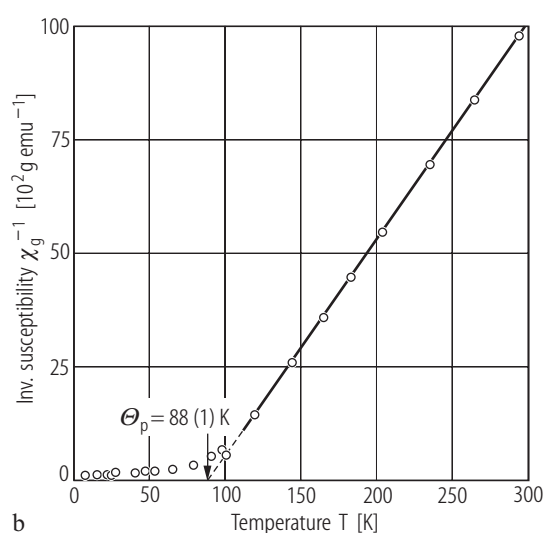
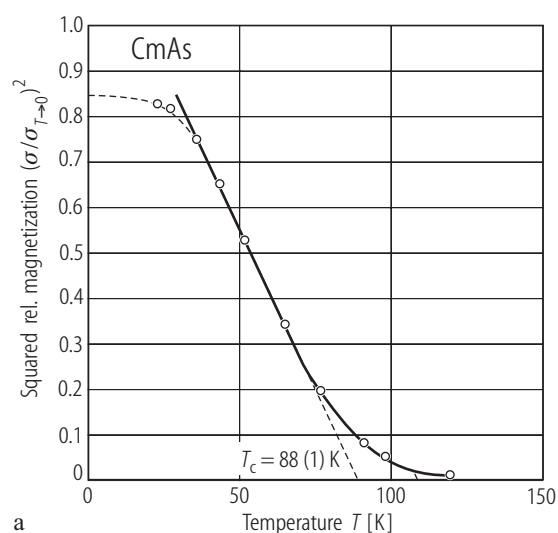


**Fig. IV.127.** CmAs. **(a)** The ratio of squared magnetizations,  $(\sigma(T)/\sigma_{T \rightarrow 0})^2$ , vs. temperature,  $T$ , [76KCM]. Extrapolation of this ratio to zero (dashed line) defines the Curie temperature  $T_C = 88(1)$  K. **(b)** Inverse specific susceptibility  $\chi_g^{-1}$  vs. temperature,  $T$  [76KCM].  $p_{\text{eff}} = 6.58$   $\mu_B$ ,  $T_C \equiv \Theta = 88(1)$  K.